

Heat Transfer and Pressure Drop in a Developing Channel Flow with Streamwise Vortices

K. C. Felton and A. M. Jacobi

ACRC TR-106

September 1996

For additional information:

Air Conditioning and Refrigeration Center
University of Illinois
Mechanical & Industrial Engineering Dept.
1206 West Green Street
Urbana, IL 61801

(217) 333-3115

*Prepared as part of ACRC Project 40
Vortex-Induced Air-Side Heat Transfer Enhancement
in Air-Conditioning and Refrigeration Applications
A. M. Jacobi, Principal Investigator*

The Air Conditioning and Refrigeration Center was founded in 1988 with a grant from the estate of Richard W. Kritzer, the founder of Peerless of America Inc. A State of Illinois Technology Challenge Grant helped build the laboratory facilities. The ACRC receives continuing support from the Richard W. Kritzer Endowment and the National Science Foundation. The following organizations have also become sponsors of the Center.

Amana Refrigeration, Inc.
Brazeway, Inc.
Carrier Corporation
Caterpillar, Inc.
Copeland Corporation
Dayton Thermal Products
Delphi Harrison Thermal Systems
Eaton Corporation
Ford Motor Company
Frigidaire Company
General Electric Company
Lennox International, Inc.
Modine Manufacturing Co.
Peerless of America, Inc.
Redwood Microsystems, Inc.
The Trane Company
Whirlpool Corporation

For additional information:

*Air Conditioning & Refrigeration Center
Mechanical & Industrial Engineering Dept.
University of Illinois
1206 West Green Street
Urbana IL 61801*

217 333 3115

Abstract

Experiments to assess the heat transfer and pressure-drop effects of delta-wing vortex generators placed at the entrance of developing channel flows are reported in this study. The experimental geometry simulates common heat exchanger configurations and tests are conducted over a velocity range important to heating, air conditioning and refrigeration. An innovative liquid-crystal thermography technique is used to determine the local and average Nusselt numbers for an isoflux channel wall, and conventional methods are used to determine the Fanning friction factor. Vortex generators with aspect ratios of $\Lambda = 2$ and $\Lambda = 4$ are studied at attack angles of $\alpha = 20^\circ$ to 45° . The results indicate that the streamwise vortices generated by a delta wing can enhance local Nusselt numbers by more than 200% in a developing channel flow. Under some conditions, the spatially average Nusselt number nearly doubled for a heat transfer area that was 37 to 63 times the wing area. The Fanning friction factor increased by a few percent to nearly 60%, depending on the Reynolds number.

Table of Contents

Chapter		Page
	List of Figures -----	vii
	List of Tables -----	x
	Nomenclature-----	xi
1	Introduction -----	1
1.1	Background and Problem Description -----	1
1.2	Literature Review -----	3
1.2.1	<u>Introduction</u> -----	3
1.2.2	<u>Vortex Generators</u> -----	4
1.2.3	<u>Enhanced Heat Transfer</u> -----	6
1.2.3.1	<u>Vortex Generators for Heat Transfer Enhancement</u> -----	6
1.2.3.2	<u>Vortex Generators in Channel Flows</u> -----	8
1.2.4	<u>Thermochromic Liquid Crystals</u> -----	10
1.2.4.1	<u>Introduction</u> -----	10
1.2.4.2	<u>Human Observation</u> -----	11
1.2.4.3	<u>Intensity-Based Image Processing</u> -----	12
1.2.4.4	<u>True-Color Image Processing</u> -----	13
1.3	Present Method and Summary of Project Objectives -----	14
2	Experimental Methods and Facilities -----	25
2.1	Wind Tunnel and Test Section -----	25
2.1.1	<u>Wind Tunnel</u> -----	25
2.1.2	<u>Test Section and Test Model</u> -----	26
2.2	Instrumentation and Data Acquisition -----	26
2.3	Heat Transfer, Pressure Drop Penalty and Velocity Measurements -----	27
2.3.1	<u>Heat Transfer Measurements</u> -----	27
2.3.2	<u>Pressure Drop Penalty Measurements</u> -----	29
2.3.3	<u>Test Section Velocity Measurements</u> -----	29
2.4	Digitizing Equipment-----	29

Chapter	Page
3 Results and Discussion -----	36
3.1 Liquid Crystal Thermography -----	36
3.2 Summary of Experimental Conditions -----	37
3.3 Average Heat Transfer Enhancement -----	37
3.4 Local Heat Transfer Enhancement -----	40
3.5 Local Temperature Profile -----	42
3.6 Pressure Drop Penalty -----	43
4 Conclusions and Future Work -----	60
4.1 Conclusions -----	60
4.2 Future Work -----	63
 APPENDICES	
A Experimental Methods for Liquid Crystal Thermography -----	65
B Procedure for Developing a Color-Temperature Lookup Table -----	69
C Data Reduction Procedure and Uncertainty Analysis -----	74
D Non-Dimensional Data -----	82
E Vortex Generator Geometry Selection -----	86
 LIST OF REFERENCES -----	 88

List of Figures

Page

Figure 1.1 - Compact heat exchanger cores: (a) flat tubes with continuous plates, (b) circular tubes with continuous plates, (c) circular tubes with circular fins[1].-----	16
Figure 1.2 - Compact heat exchangers cores: (a) interrupted fins, and (b) triangular continuous fins[3].-----	17
Figure 1.3 - Example of vortex generators on a flat plate[4].-----	18
Figure 1.4 - Typical core of a gas-liquid tube-fin heat exchanger[3]. -----	19
Figure 1.5 - Typical core of a gas-gas plate-fin heat exchanger[3].-----	20
Figure 1.6 - Cross section of primary and secondary vortices for flow over a delta wing[13]. -----	21
Figure 1.7 - Frontal view of trailing vortices from an aircraft wing[10].-----	22
Figure 1.8 - Spanwise lift distribution across a delta wing resulting from the primary and secondary vortices[13]. -----	23
Figure 1.9 - Mirror image of a typical vortex interacting with a flat wall[12].-----	24
Figure 2.1 - Sketch of wind tunnel used in this study. -----	31
Figure 2.2 - Sketch of prototype heat exchanger used in this study. -----	32
Figure 2.3 - Sketch of center test fin used in this study. -----	33
Figure 2.4 - Plot of mean test section velocity versus test section position. -----	34
Figure 2.5 - Schematic of computer and digitizing equipment used to digitize 35mm color negatives. -----	35
Figure 3.1 - Plot of color table position versus surface temperature for TLC surface.-----	44
Figure 3.2 - Example of lift versus angle of attack for a delta wing in freestream velocity with an aspect-ratio range of .83 to 3.97[12]. -----	45
Figure 3.3 - Example of lift versus angle of attack for a rectangular wing in freestream velocity with an aspect-ratio range of 1.0 to 7.0 [10].-----	45

Figure 3.4 - Average Nusselt number ratio (enhanced to unenhanced) versus angle of attack for a delta-wing VG with an $\Lambda = 2.0$. -----	46
Figure 3.5 - Average Nusselt number ratio (enhanced to unenhanced) versus angle of attack for a delta-wing VG with an $\Lambda = 4.0$. -----	47
Figure 3.6 - Local temperature profile of heat transfer surface with a delta wing vortex generator at the leading edge ($\Lambda = 2.0$, $\alpha = 45$ deg, $Re = 5200$). The colors represent the following approximate temperatures: red (30.2 C), green (32.0 C), blue (35.8C)-----	48
Figure 3.7 - Local temperature profile of heat transfer surface with a delta wing vortex generator at the leading edge ($\Lambda = 2.0$, $\alpha = 45$ deg, $Re = 6300$). The colors represent the following approximate temperatures: red (30.2 C), green (32.0 C), blue (35.8 C)-----	49
Figure 3.8 - Local temperature profile of heat transfer surface with a delta wing vortex generator at the leading edge ($\Lambda = 4.0$, $\alpha = 45$ deg, $Re = 5200$). The colors represent the following approximate temperatures: red (30.2 C), green (32.0 C), blue (35.8 C). -----	50
Figure 3.9 - Local temperature profile of heat transfer surface with a delta wing vortex generator at the leading edge ($\Lambda = 4.0$, $\alpha = 45$ deg, $Re = 6300$). The colors represent the following approximate temperatures: red (30.2 C), green (32.0 C), blue (35.8 C). -----	51
Figure 3.10 - Local spanwise heat transfer enhancement that was produced by a delta-wing VG; VG conditions were $\Lambda = 2.0$, $\alpha = 30$ degrees, $Re = 5200$. -----	52
Figure 3.11 - Local spanwise heat transfer enhancement that was produced by a delta-wing VG; VG conditions were $\Lambda = 4.0$, $\alpha = 30$ degrees, $Re = 5200$. -----	53
Figure 3.12 - Local spanwise heat transfer enhancement that was produced by a delta-wing VG; VG conditions were $\Lambda = 2.0$, $\alpha = 30$ degrees, $Re = 6300$. -----	54
Figure 3.13 - Local spanwise heat transfer enhancement that was produced by a delta-wing VG; VG conditions were $\Lambda = 4.0$, $\alpha = 30$ degrees, $Re = 6300$. -----	55
Figure 3.14 - Fanning friction factor versus Re for a delta-wing VG with an $\Lambda = 2.0$.---	56
Figure 3.15 - Fanning friction factor versus Re for a delta-wing VG with an $\Lambda = 4.0$ ---	57

Figure 3.16 - Friction factor ratio versus Re for a delta-wing VG with an $\Lambda = 2.0$. -----	58
Figure 3.17 - Friction factor ratio versus Re for a delta-wing VG with an $\Lambda = 4.0$..-----	59
Figure A.1 - Plot of thermocouple readings for color-temperature calibration. -----	68
Figure B.1 - Sample RGB color model[48].-----	72

List of Tables

	Page
Table 3.1 - Summary of Delta-Wing Geometry and Experimental Conditions-----	37
Table 3.2 - Summary of Dimensions for Delta-Wing to Heat Transfer Surface Area Ratio -----	38
Table 3.3 - Summary of Selected Local Approximate Enhancement Values -----	41
Table 4.1 - Impact of Wing-Type Vortex Generators on the Performance of a Simplified Continuous-Fin Heat Exchanger -----	62
Table B.1 - RGB Mean and Standard Deviation Values for TLC Surface -----	73
Table E.1 - Summary of Delta-Wing Geometry and Experimental Conditions -----	86

Nomenclature

A, A_{ht}	surface area of heat transfer surface
A_c	prototype heat exchanger minimum flow cross sectional area
A_{DW}	delta-wing surface area
A_{HTS}	heat transfer surface area used in image analysis
A_{op}	area of orifice plate
A_{ts}	cross sectional area of wind tunnel test section
b	wing span
b	blue component of color vector for reference RGB values
b_i	blue component of color vector for new image
c	chord length of wing
c_l	lift coefficient
c_p	specific heat at constant pressure
C	discharge coefficient
CTP	color table position
d^2	Euclidean distance
D_h	hydraulic diameter
D_{op}	diameter of orifice plate
D_p	diameter of pipe for mass flow meter
f	Fanning friction factor, $(\Delta p D_h / 2 \rho U_c^2 L)$
g	green component of color vector for reference RGB values
g_i	green component of color vector for new image

$h(x,y)$	local heat transfer coefficient
\bar{h}	average heat transfer coefficient
H	height of prototype heat exchanger fin
H_l	heater length
H_w	heater width
k_f	thermal conductivity of the fluid
K	flow coefficient
L	length of prototype heat exchanger and fin
L_c	characteristic length
\dot{m}_{op}	mass flow rate
N_p	number of plate fins in prototype heat exchanger
$Nu(x,y)$	local Nusselt number, $(q_s'' D_h / \Delta T k_f)$
\overline{Nu}	average Nusselt number, $(q_s'' D_h / \Delta \bar{T} k_f)$
Nu_{enh}	enhanced Nusselt number
Nu_o	unenhanced Nusselt number
Nur	Nusselt number ratio
P	pressure
Pe	Peclet number, $(RePr)$
Pr	Prandtl number
q_s''	surface heater heat flux
r	red component of color vector for reference RGB values

r_i	red component of color vector for new image
Re	Reynolds number, $(U_c D_h / \nu_a)$
S	surface area of vortex generator
$T_s(x,y)$	local surface temperature
T_{HB}	temperature of higher bound of thermochromic liquid crystal activation
T_{LB}	temperature of lower bound of thermochromic liquid crystal activation
T_m	mean or bulk fluid temperature
T_s	surface temperature
$\overline{T_s}$	average surface temperature
u,v,w	velocity
U,V,W	non dimensional velocity
U_∞	freestream velocity
U_c	mean channel flow velocity
x,y,z	coordinates
X,Y,Z	dimensionless positions for coordinates
X^*	nondimensional streamwise position, $(x/D_h Pe)$
Y^*	nondimensional spanwise position, $(2y/H_w)$
α	angle of attack or angle of incidence
β	diameter ratio
Δp	pressure difference
ΔT	temperature difference
$\overline{\Delta T}$	average temperature difference

Λ aspect ratio of vortex generator, (b^2/S)

δ_p test fin thickness

ρ_a density of air

θ dimensionless temperature

μ dynamic viscosity

ν_a kinematic viscosity

Chapter 1 - Introduction

1.1 Background and Problem Description

The desire for improved heat exchanger performance has led to various heat transfer augmentation techniques. The objective of these augmentation methods is to reduce the initial cost of the heat exchanger or to reduce its operating cost. Initial cost can be reduced if the heat transfer augmentation allows a reduction in heat-exchanger weight or volume. Operating cost can be reduced if the augmentation allows the heat exchanger to meet the heat duty requirements with a lower pressure drop.

Heat transfer enhancement techniques are typically classified as passive or active. Passive techniques do not require direct application of external power other than pumping power, but active techniques require external power; examples of active techniques include rotating and vibrating heat transfer surfaces, pulsating fluids, and the introduction of electric fields. Passive augmentation methods usually offer the advantages of less complexity, lower capital cost, and higher reliability. Passive techniques often focus on extended surface design (i.e. fin design).

Tube-fin and plate-fin geometries are examples of heat exchangers with extended surfaces (fins). In figure 1.1, common arrangements of tube-fin (circular and flat) heat exchangers are shown; the gas flows between the fins while the liquid flows inside the tubes. Webb[2] has documented that the gas-side heat transfer coefficient is 10 to 50 times smaller than the liquid side for gas-to-liquid heat exchangers. The primary purpose of the fin is to increase the gas-side heat-transfer surface area, resulting in a lower air-side thermal resistance. Typical plate-fin constructions are shown in figure 1.2, where two types of fins - continuous and interrupted - are also shown. When plain fins are straight along the flow path (as in figure 1.2b) the flow development (growth of the boundary layers) results in a lower heat transfer coefficient than for cases where the surface is interrupted. Some alternative designs (e.g., wavy fins) use vortex shedding to produce

thinner boundary layers, resulting in a higher heat transfer coefficient. However, according to Sukhatme and Devota[3], the interrupted surface provides superior heat transfer performance. Near the leading edge of the fin, the value of the heat transfer coefficient is high; it decreases downstream from the leading edge. Each break in an interrupted surface restarts the leading-edge condition, resulting in a higher heat transfer coefficient than a continuous flat plate. The increase in heat transfer from wavy and interrupted fins is achieved at the expense of increased pressure drop, resulting in a higher pumping power requirement for the fan.

Vortex-induced heat transfer enhancement is one method of augmenting the gas-side heat transfer coefficient with a potentially lower pressure drop penalty than wavy or interrupted fins. Vortex-induced heat transfer enhancement is accomplished by the introduction of streamwise vortices in the flow field. Mounting delta wings or winglet type vortex generators on a channel wall, as shown in figure 1.3, is one means of creating these vortices. For a delta-wing vortex generator, vortices are developed as a result of the pressure difference between the high-pressure (up stream) and the low-pressure (down stream) wing surface. The streamwise vortices interact with the otherwise two-dimensional developing channel flow to produce a three-dimensional swirling flow that mixes the core fluid with the near-wall fluid. Mixing enhances the heat transfer by effectively thinning the thermal boundary layer[4, 5]. In contrast to wavy and interrupted fins, this enhancement technique offers the potential of modest pressure losses. According to Batchelor[6], a delta wing has the potential for modest pressure losses because the form drag for such wing-type slender bodies is low.

This study represents an evaluation of the heat transfer augmentation potential of vortex generators, with a focus on delta-wing geometries in channel flows. The pressure losses associated with delta wings will be determined experimentally.

1.2 Literature Review

1.2.1 Introduction - For a viscous fluid flowing inside a channel or duct, a thin momentum boundary layer forms along the inner wall. In the case where heat transfer occurs between the channel wall and fluid, a thin thermal boundary also forms along the inner walls of the channel. When a boundary layer is present, flow over a body or flow inside a channel can be divided into two fluid regions: (1) a very thin layer near the wall, where the velocity and temperature gradients are steep and (2) a region outside of the boundary layer known as the external-flow or core-flow region, where the velocity and temperature gradients are small. The velocity and temperature profiles are uniform at the entrance of a channel and in the core fluid section. The thickness of the velocity and thermal boundary layers increases with distance from the duct entrance.

The region where the velocity profile is still developing is designated as the velocity or hydrodynamic entrance region. The region beyond this entrance section is known as the hydrodynamically fully-developed region. Similarly, the region where the temperature profile is developing is known as the thermal entrance region. At a certain location downstream of the channel inlet, the thermal boundary layers meet; a small distance downstream of this point the flow is considered thermally fully-developed.

The central focus of this study is the use of vortex generators as a heat transfer augmentation technique for developing channel flows. Vortex generators, such as those shown in figure 1.3, reduce the thermal boundary layer thickness leading to enhanced heat transfer in the developing region and a longer development length. In the fully developed region, they create a swirl flow that increases the bulk fluid mixing and heat transfer. Experimental investigations by Fiebig et al.[7], Russell et al.[8], and Tiggelbeck et al.[9] have shown high potential for applying vortex generators, such as delta wings and winglets, to enhance the gas-side heat transfer coefficient. Two heat exchanger geometries that may benefit from this heat transfer augmentation method are shown in figures 1.4 and 1.5.

In this literature review, published reports related to vortex-induced heat transfer enhancement and to liquid crystal thermography, a method for interpreting color-temperature relations of thermochromic liquid crystals (TLCs), will be discussed. First, a summary of research related to vortex generators as a boundary layer control method is presented. This section is followed by a review of vortex generators as a heat-transfer enhancement tool for both flat-plate and channel-flow configurations. Lastly, a brief history of various techniques for liquid crystal thermography is presented.

1.2.2 Vortex Generators - There have been a number of studies examining the use of vortex generators (VG) to delay separation[10]. Lachmann[11] reported that the first recorded study of boundary layer control was performed in 1904 by Prandtl. Immediately following the development of boundary layer theory, Prandtl proceeded to demonstrate how separation could be prevented by removing fluid from the boundary layer. However, it took about a half century before the aircraft and its powerplant technology had sufficiently matured to make practical application of the concept of boundary layer control. Between 1904 and 1914 fewer than ten journal articles related to the boundary layer were published. By 1954, the number of boundary-layer related journal articles had increased significantly to 120 annually, indicating a huge growth of interest in this area. Since the benefit of applying boundary layer control for improved aircraft design resulted in higher wing performance, the prime reason for the increase in research interest in the 1950s was the use of boundary layer control for advancing aircraft wing technology[11].

Aerodynamicists have investigated various wing geometries - geometries with high and low-aspect ratio wings - to improve aircraft wing design and influence boundary layer separation. The use of vortex generators (both active and passive) has been researched by the aircraft industry as a means of delaying separation. According to Kuethe and Chow[10], Taylor and Bruynes invented the first vortex generators for aircraft wing applications. The generators consisted of an array of vanes normal to the surface and

projecting to the edge of the boundary layer; adjacent vanes were canted differently so that the tips would generate a layer of counter-rotating streamwise vortices. These vortices with streamwise axes were superimposed on the natural turbulent boundary layer to provide an additional eddy viscosity. The enhanced mixing enabled the flow to remain attached well beyond the separation point for the natural turbulent layer. Once generated, the vortices persisted downstream in excess of one hundred times the boundary layer thickness. Mixing the flow provides enhanced heat transfer and increased skin friction. However, according to Kuethe and Chow[10], experimental investigations by Thwaites at NACA demonstrated that the application of generators increased the maximum lift coefficient ($c_{l,max}$) by 48% with only a slight increase in the drag coefficient. The heat transfer augmentation provided by vortex generators is the central focus of this study.

In addition to vortex generators, various wing geometries have been experimentally investigated to determine the impact of the wing geometry on the trailing vortex strength. One wing geometry that has been studied extensively is the delta wing, particularly in relation to the streamwise ('trailing') vortices. The physics of the formation of vortices along the delta wing has been well documented[12]. The flow field pattern over the top of a delta wing at an angle of attack (see figure 1.6) is dominated by two vortex patterns (primary and secondary vortices)[13]. These patterns occur in the vicinity of the highly swept leading edges and are created by the following mechanism. Pressure on the bottom surface of the wing, facing the flow field at the angle of attack, is higher than the pressure on the top surface. This pressure difference forces the fluid to leak over the edges from the high-pressure to the low-pressure side, resulting in well-ordered streamwise vortices along the wing and in the wake region. This swirling flow (vortices) induces a downward component of velocity, known as downwash, on the wing surface and in the wake region. This downwash velocity is proportional to the vortex strength (circulation)[14].

Looking in the direction of flight, the left wing tip produces a vortex that rotates clockwise, while the right wing tip produces a counter-clockwise vortex (figure 1.7).

Research by Wentz and Kohlman[15] has shown that vortex size and strength along the upper surface of a delta wing increases with angle of attack. Figure 1.8 shows the lift distribution along the upper surface of a delta wing for primary and secondary vortices. These vortices generate high velocities particularly at the core, resulting in low pressure regions on the upper surface. Kuethe and Chow[10] have documented that lift is proportional to circulation and velocity squared; therefore, higher lift can be accomplished by increasing circulation.

Regarding the use of delta wings as a heat transfer enhancement mechanism, the downwash velocity (behind the delta wing) thins the thermal boundary, resulting in an increase in heat transfer. This concept will be discussed in greater detail in the following section.

1.2.3 Enhanced Heat Transfer

1.2.3.1 Vortex Generators for Heat Transfer Enhancement - Lachmann[11] reported that the initial use of vortex generators was exclusively for boundary layer control. Nevertheless, the heat transfer community has recently begun exploring vortex generation as a heat transfer enhancement technique. In 1969, the first archival article on the use of vortex generators for enhanced heat transfer appeared in the literature. Johnson and Joubert[16] studied a right circular cylinder in crossflow with delta winglet vortex generators attached on the cylinder at a specified angle of attack. The measured local heat transfer increased by as much as 200%, but the average heat transfer coefficient was lowered due to decreases in the other regions on the cylinder. Local enhancements were due to the increase in mixing, while the reduced average values were due to the diminishing impact of recirculation eddies behind the cylinder.

A study by Kataoka et al.[17] clarified the mechanisms for local heat transfer enhancement. They experimentally investigated the local behavior of an inner rotating cylinder and outer stationary cylinder with an imposed axial velocity in the annulus. This

test configuration resulted in a system of Taylor vortices. Measurements of the local heat transfer indicated that the prime mechanism for heat transfer enhancement was due to a flow toward the heat transfer surface (a downwash flow) induced by neighboring vortices. Conversely, in regions where the vortices induced an outflow (an upwash) a decrease in heat transfer was recorded. These results imply that heat transfer augmentation was related to local thinning of the thermal boundary. Since delta wings produce counter-rotating vortices (as discussed in section 1.2.2), one could infer that this geometry would generate vortices that would enhance heat transfer.

In the mid seventies, Edwards and Alker[18] compared surface-mounted cubes and delta-winglet vortex generators in a duct flow configuration and found that delta winglets, which produce counter-rotating vortices, resulted in better overall heat transfer enhancement. Locally the enhancement produced by delta winglets was not as high as the cube, but the enhancement persisted much further downstream. They also noted that counter-rotating vortices performed better than co-rotating vortices. About ten years later, Russell et al.[8] reported on an evaluation of various vortex generator configurations, and after considering delta and rectangular winglets in a full-scale flat-tube heat exchanger, they found a rectangular winglet in two staggered rows to be the most promising (see figure 1.3 for an example of a rectangular wing). At a Reynolds number of 500, the j factor increased by 47% whereas the friction factor (f) increased by only 30%. The results were more encouraging at higher speeds; for a Reynolds of 1000 the j factor increased by 50% and the f factor increased by only 20%. For a flat plate configuration, Turk and Junkhan[19] also investigated rectangular winglets and reported the heat transfer results by comparing the ratio of Nusselt number of the enhanced surface (Nu_{enh}) to the unenhanced surface (Nu_o). They found that the spanwise average Nusselt number ratio, $\overline{Nu}_{enh}/\overline{Nu}_o$, increased in the streamwise distance. In other words, the heat transfer decreased at a slower rate for the enhanced surface than the unenhanced surface.

Eibeck and Eaton[20] conducted a study of the heat transfer effects of a single longitudinal vortex embedded in a turbulent boundary layer on a flat plate. Interaction of the vortex

with the wall caused the vortex to be distorted as shown in figure 1.9. A single longitudinal vortex interacts with the wall as if it is interacting with a mirror image of itself in the wall. The vortex and its image mutually induce a spanwise velocity. The measured heat transfer increase reported by Eibeck and Eaton[20] was 25% for downwash flow (flow toward the wall), and a heat transfer decrease of 15% was measured for the upwash flow.

1.2.3.2 Vortex Generators in Channel Flows - There has been considerable interest during the last five years in the use of vortex generators for heat transfer enhancement in channel flow configurations. Fiebig and co-workers have made significant contributions in this area using both numerical and experimental methods[21-26]. Their published experimental results have been based on unsteady liquid crystal thermography and drag force measurements.

Zhu et al.[21] performed a numerical analysis of the effects of longitudinal vortices in turbulent channel flows. Four vortex-generator geometries (delta wing, rectangular wing, delta winglet pair and rectangular winglet pair) were studied. Similar to the results reported for heat transfer enhancement on flat plates, Zhu et al.[21] found that strong longitudinal vortices are produced when objects such as wings and winglets were placed in the flow stream. These results showed that longitudinal vortices elevated the turbulent kinetic energy and disrupted the growth of the thermal boundary layer. The mean heat transfer rate increased by as much as 28% for a channel-wall area 30 times larger than the vortex generator area. Measurements of the local heat transfer behavior revealed that the delta and rectangular wing geometries produced large differences in maximum and minimum heat transfer enhancement. The rectangular wing produced the highest heat transfer enhancement. However, when the heat transfer behavior and flow losses were considered the rectangular winglet pair was superior.

In 1989, Fiebig et al.[22] performed a numerical investigation focusing on the temperature and velocity structure produced by wing and winglet vortex generators in a channel flow.

Their findings corroborated earlier research by demonstrating that these vortex-generator geometries produced counter-rotating longitudinal vortices. In contrast to vortices produced in a flat plate configuration, they found that vortices in channel flows showed an elliptic deformation due to the channel walls. They also noted an absence of vortex breakdown at wing angles of attack as high as 50 degrees, which the authors attribute to a favorable pressure gradient of a channel flow[22]. Results from flat plate studies have shown vortex breakdown to occur for delta-wing angle of attacks as low as 27 degrees[7] .

Complimentary to the numerical studies described above, a number of reports documenting experimental research have been published related to vortex-induced heat transfer enhancement in channel flows. Fiebig et al.[22, 23] investigated the impact of a single vortex generator on flow structure, flow losses, and heat transfer rate. The vortex generators (delta and rectangular wings) were formed by punching small sections out of flat-plate fins so that they protruded into the main flow at an angle of attack. The fins were mounted on top of each other to form channels for a plate-fin heat exchanger. Similar to the numerical study by Zhu et al.[21], Fiebig and co-workers[23] measured stable vortices for a wing at an angle of attack as high as 50 degrees. The mean heat transfer increased by approximately 50% for an angle of attack of 50 degrees and Reynolds range of 1000 to 2000. In general, the heat transfer increased with angle of attack and was independent of Reynolds number in the range investigated. According to Fiebig et al.[23], the best performing geometry on a per unit vortex generator area basis was the delta wing, closely followed by the delta winglets and delta winglet pairs.

In a similar study, Tiggelbeck and co-authors[24] investigated single and double rows of delta winglet pairs in the transition to turbulent flow regime. The winglets were punched out of a series of parallel plates that formed channel walls and they protruded into the flow to create longitudinal vortices. The unsteady liquid crystal technique aided by the use of a laser projecting on the heat transfer surface was employed to measure the surface temperature and visually analyze the flow structures. The location of the second row of generators influenced the peak and average heat transfer increase. When the ratio between the distance separating the wings and channel height reached 7, the heat transfer

enhancement approached a constant value. For a Reynolds number of 5600, the average heat transfer increased by 77% with two aligned rows of generators.

Tiggelbeck et al.[25] did later research, comparing aligned and staggered double-row delta winglets. Employing the unsteady liquid crystal technique, they found that aligned winglets performed better than staggered winglets. Local heat transfer augmentation measurements showed increases of several hundred percent for an angle of attack of 45 degrees; the average enhancement was 80% for $Re = 6000$, while the drag simultaneously increased by 165%.

The literature summarized above indicates that vortex generators are an effective tool for enhancing heat transfer in both flat-plate and channel-flow configurations and are well suited for gas-to-liquid heat exchangers. A more thorough review on the subject of vortex-induced heat transfer enhancement has been presented by Jacobi and Shah[4] and Fiebig[26].

1.2.4 Thermochromic Liquid Crystals

1.2.4.1 Introduction - Researchers often use thermocouples to obtain accurate surface temperature measurements; however, thermocouples are intrusive, and for large surface areas, numerous thermocouples are required to obtain a high-resolution thermal map. Alternate techniques for obtaining high-resolution temperature maps are infrared sensing and temperature-sensitive phosphors. Infrared thermometry is expensive and requires special wind tunnel material[27]; phosphors must be viewed under an ultraviolet light to show fluorescence and often provide poor resolution[27]. Another technique uses thermochromic liquid crystals as a temperature measuring tool. Promising results have been reported for both surface and volume-distributed-measurements, without the drawbacks of the above mentioned techniques[28].

Liquid crystals were discovered by Friedrich Reintizer[29] in 1888, but their industrial usage did not occur until the 1960s with the advent of the of electronic display devices.

About a decade later, researchers began to use thermochromic liquid crystals (TLCs) as a temperature-measuring tool. Thermochromic liquid crystals offer the following advantages over thermocouples:

1. They can be easily applied and are low cost when compared to thermocouples.
2. They are nonintrusive to the flow field and heat transfer surface.
3. They offer accurate temperature measurement and high resolution.
4. The temperature measurement is nearly instantaneous and the color display is reversible.

The impetus for growth in the use of TLCs in heat transfer studies has been advances in personal computers, image processing equipment, and encapsulation and application techniques of liquid crystals.

The process of interpreting color images from thermochromic liquid crystals is known as liquid crystal thermography (LCT), and there are three broad classes of image interpretation techniques: human observation, intensity-based image processing, and true-color image processing.

1.2.4.2 Human Observation - Human observation is extremely effective in obtaining qualitative information but is weak in obtaining quantitative high-resolution temperature maps. In addition, it is subjective because it relies on the evaluator to interpret the temperature and color relation by viewing recorded images. Each evaluator could have a different interpretation of the color, resulting in higher uncertainty than the other two techniques - intensity-based and true-color image processing.

Several investigators have used the human observation LCT approach to interpret the color-temperature relation [27-34]. The observer interprets the images by inspecting photographs or video images and focuses on three colors (red, blue, and green) that are calibrated to particular isotherms. A temperature and heat transfer coefficient are then assigned to the three colors neglecting the transition colors; the impact of neglecting the

transition colors is lower spatial resolution. In implementing the approach that uses a single isotherm, the surface flux is varied with a single frame recorded at each surface flux value. These images are then overlayed to develop a full-field temperature map. Hippensteele[30] studied turbine cooling techniques with TLCs using this single color approach to map the temperature profile on a turbine blade. Cooper and Groff[32] investigated the heat required to produce clinical lesions and used human observation LCT to develop the temperature map. Simonich and Moffat[33] documented that an observer with little experience using 1/3 of the color-play temperature band could obtain an uncertainty of $\pm .2$ to $.5$ degree C. Intensity-based LCT approaches can produce a lower uncertainty if a narrow-band temperature TLC is used.

1.2.4.3 Intensity-Based Image Processing - The intensity-based image processing technique is less subjective than the human observation technique. Photographs are recorded using single or multiple filters that only pass light at a particular wavelength (or band). This approach produces an accurate temperature profile; however, it requires multiple frames to produce a single high-resolution temperature profile. Although it requires several images to obtain a single high-resolution temperature map, it is useful because it results in a lower uncertainty than the human observation technique.

Asforth-Frost et al.[35], using a narrow-band TLC, studied tube plate ligaments on a shell-tube heat exchanger and achieved an uncertainty of $\pm .25$ degree C. Twelve to fourteen frames were required to obtain a full thermal map. When an intensity-based LCT method is used to record a wide-band TLC, the uncertainty values are comparable to human observation. Akino et al.[36] reported an uncertainty of $\pm .5$ degree C with a wide-band TLC using a multiple filter intensity-based system, while Hollingsworth et al.[37] recorded an uncertainty of $\pm .6$ degree C. Both these investigations required multiple frames to obtain an image of the temperature and heat transfer profiles.

1.2.4.4 True-Color Image Processing - Recent advances in digital image processing equipment and high-speed personal computers have provided the opportunity to record full-field temperature measurements with a single picture frame; lower uncertainty values than intensity-based processing are also achieved. This technique is known as true-color image processing. The color display from a surface coated with TLCs is decomposed into three components, and this decomposition provides a quantitative method for analyzing color. This analysis is based on the standard mathematical representation of color used by the television and color printing industries. A detailed discussion of trichromatic color representation can be found in texts by Pratt[38] and Foley et al.[39]. Historically equipment used in recording and processing the images consisted of a color CCD camera, television and VCR, frame grabber, 24-bit monitor, and personal computer with image processing software. A liquid crystal image was recorded by the camera, digitized by the frame grabber and then stored on the computer.

Recently, researchers employing TLCs for mapping surface temperature have used the hue, saturation, intensity (HSI) color model for relating color and temperature. The three quantities -- hue, saturation, and intensity -- numerically describe the color behavior as a vector in HSI space. Research by Moffat[29] has demonstrated that the color vector can be represented using a scalar quantity if care is taken in the calibration and heat transfer experiment. Moffat[29] used hue (one coordinate in HSI space) as a scalar representation for color; hue is the dominant wavelength of the color. This approach provided good results in the middle range of the active band for the TLC; however, the temperature resolution was poor in the upper and lower third of the active color range.

Investigations by Hollingsworth et al. [40], Farina et al.[41], Lee et al.[42], and Camci et al.[43-44] have demonstrated the effectiveness of the true-color image technique. They have documented the ability to translate the colors displayed by a surface coated with TLCs into temperature values. Hollingsworth[37] et al. obtained an uncertainty of $\pm .64$ degree C in their investigation using a true-color image processing system, while Farina et al.[41] recorded an uncertainty of $\pm .25$ degree C for a full field temperature and heat

transfer profile. Camci et al.[44] have obtained the lowest documented uncertainty of $\pm .1$ degree C for a flat surface coated with TLCs. The equipment employed in the above LCT method consisted of a CCD or video camera system and related hardware described earlier in the discussion on true-color image processing.

The true-color processing method based on a hue-temperature is an effective means relating the color for the middle region of the temperature bandwidth; however, its effectiveness is reduced at the lower and upper ranges of the temperature because of the hue values are relatively uniform in the upper and lower range of the bandwidth. The color-temperature relation developed in this study addresses this weakness of the hue-temperature based approach by using a color-temperature lookup table to relate color and temperature. For this study, the color-temperature lookup table provided the color table position, temperature, and color data. The color table approach is a common method for relating colors for display on the color monitor of a computer system.

1.3 Present Method and Summary of Project Objectives

An alternative to the hue-temperature approach for mapping TLCs is the use of the full RGB color coordinate system. Similar to HSI, RGB is a color coordinate system for numerically describing color behavior. This study introduces an approach for relating color and temperature based on the three components of the RGB color vector. In order to relate the TLC colors to temperatures, the color vector data were organized in a color lookup table. Each surface temperature calibration value corresponded to a position in the color lookup table and to calibrated red, green, blue values. This approach offers one significant advantage over the hue-temperature based method; it provides good temperature resolution over the entire active color range of the TLC.

The heat transfer enhancement potential of vortex generators placed in a channel will be

determined using the color table position approach described above. The local and average surface temperature of the TLC coated surface will be determined, and these data will be used to calculate the local and average heat transfer enhancement. Lastly, the pressure losses produced by the vortex generators will be measured experimentally.

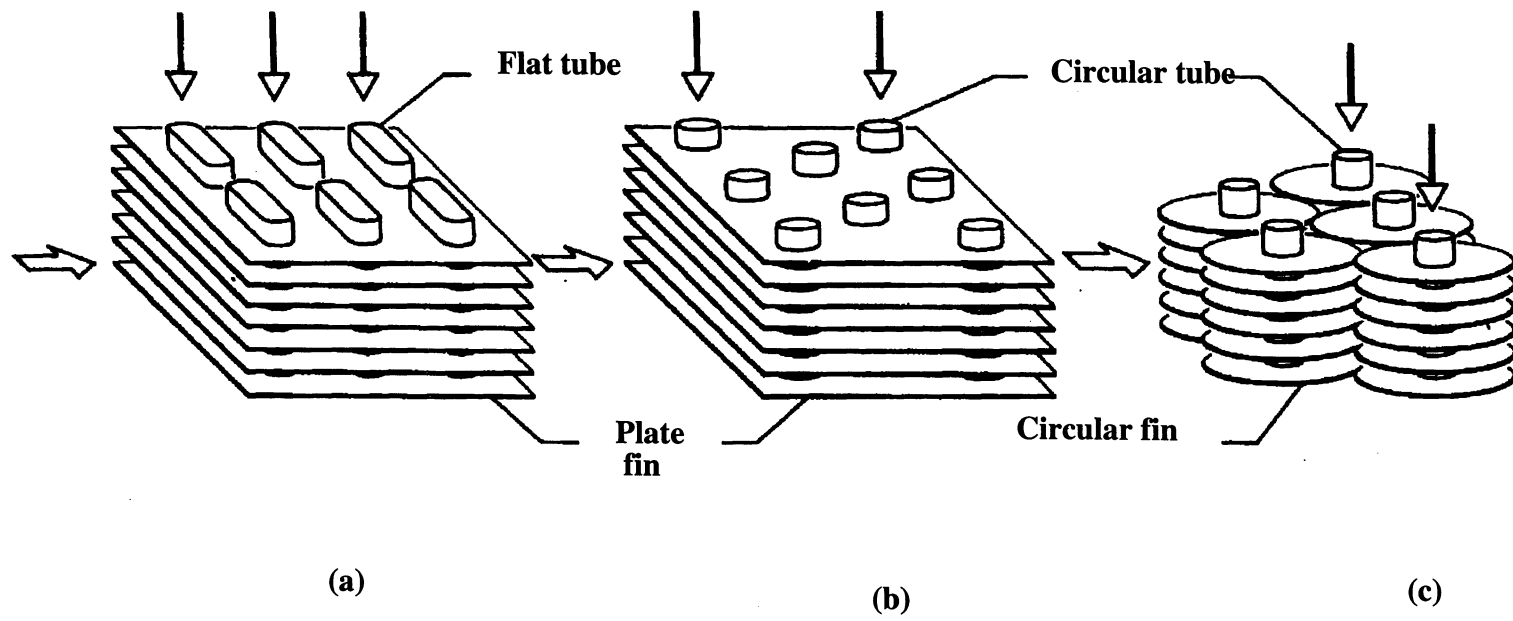
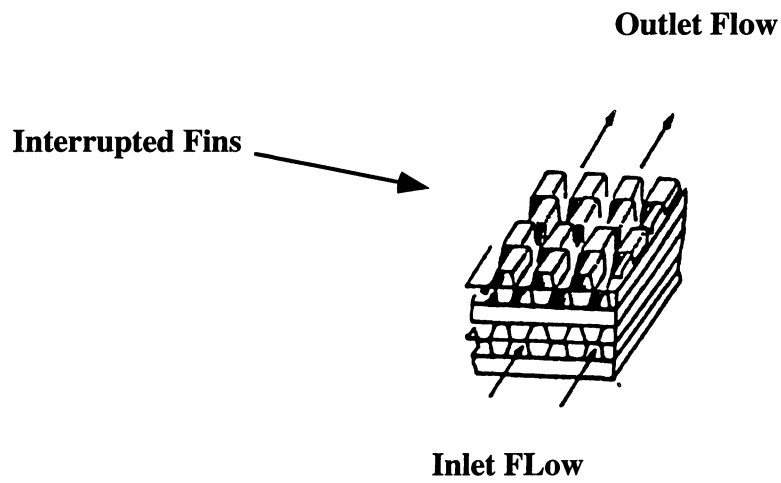
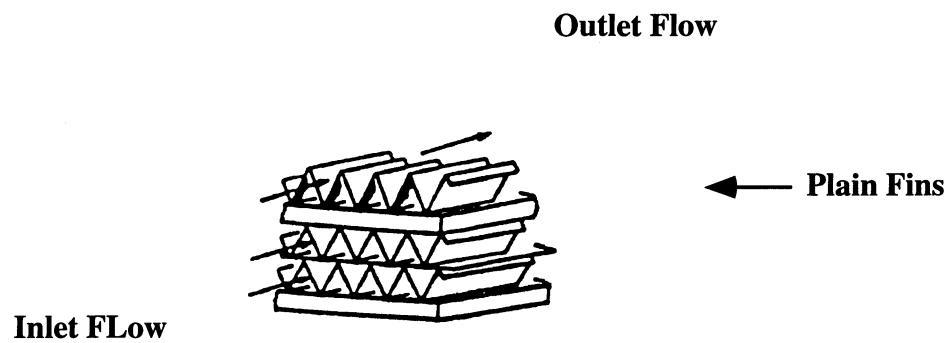


Figure 1.1 - Compact tube-fin heat exchanger cores: (a) flat tubes with continuous plate fins, (b) circular tubes with continuous plate fins, (c) circular tubes with circular fins)[1].



(a)



(b)

Figure 1.2 - Compact plate-fin heat exchanger cores: (a) interrupted fins, and (b) triangular continuous fins[3].

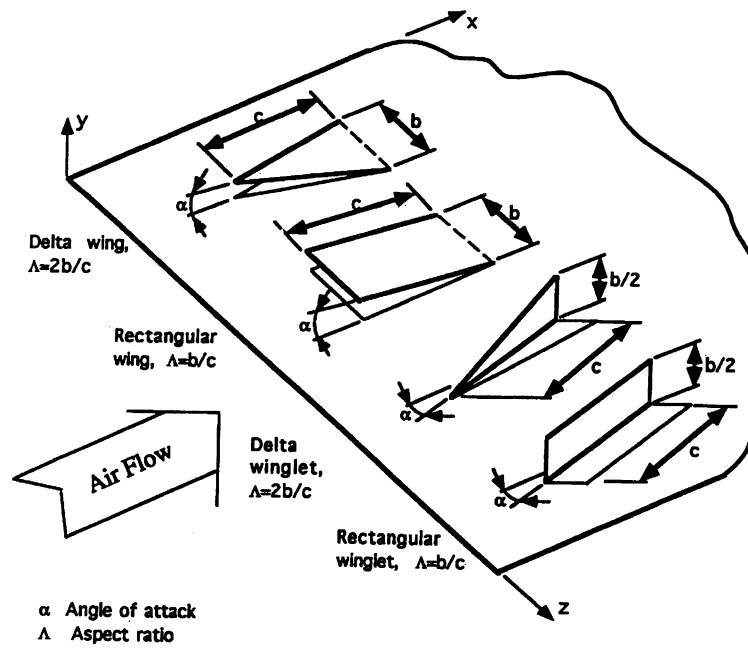


Figure 1.3 - Example of vortex generators on a flat plate[4].

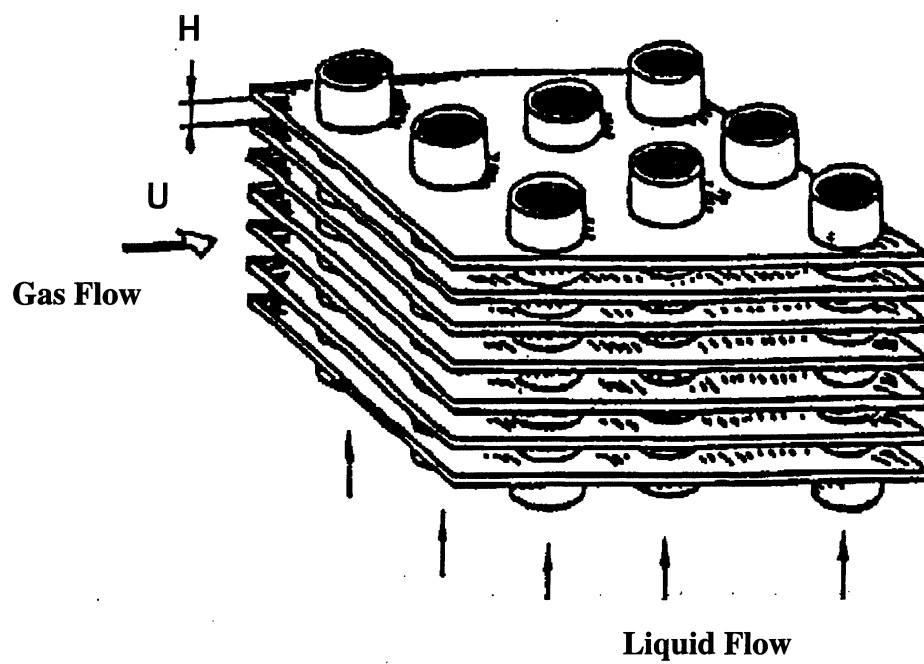


Figure 1.4 - Typical core of a gas-liquid tube-fin heat exchanger[3].

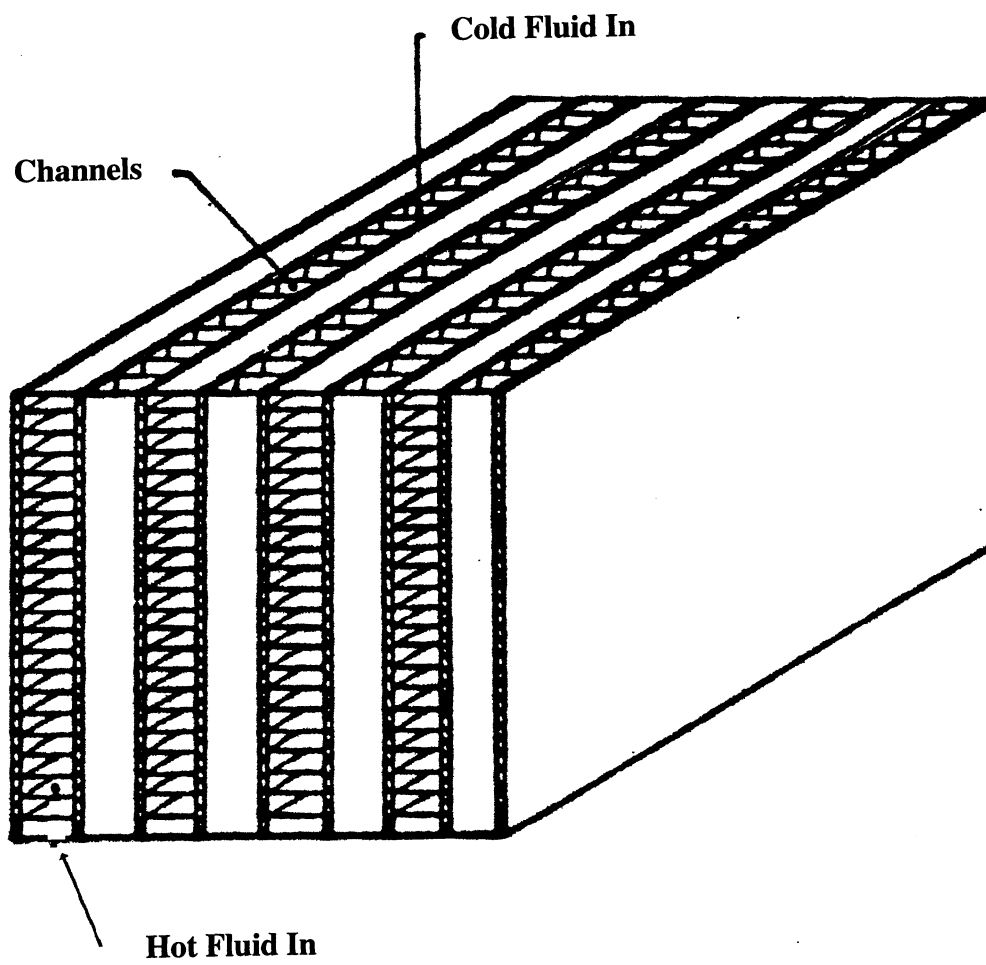


Figure 1.5 - Typical core of a gas-gas plate-fin heat exchanger[3].

**SECONDARY
VORTEX**

PRIMARY VORTEX

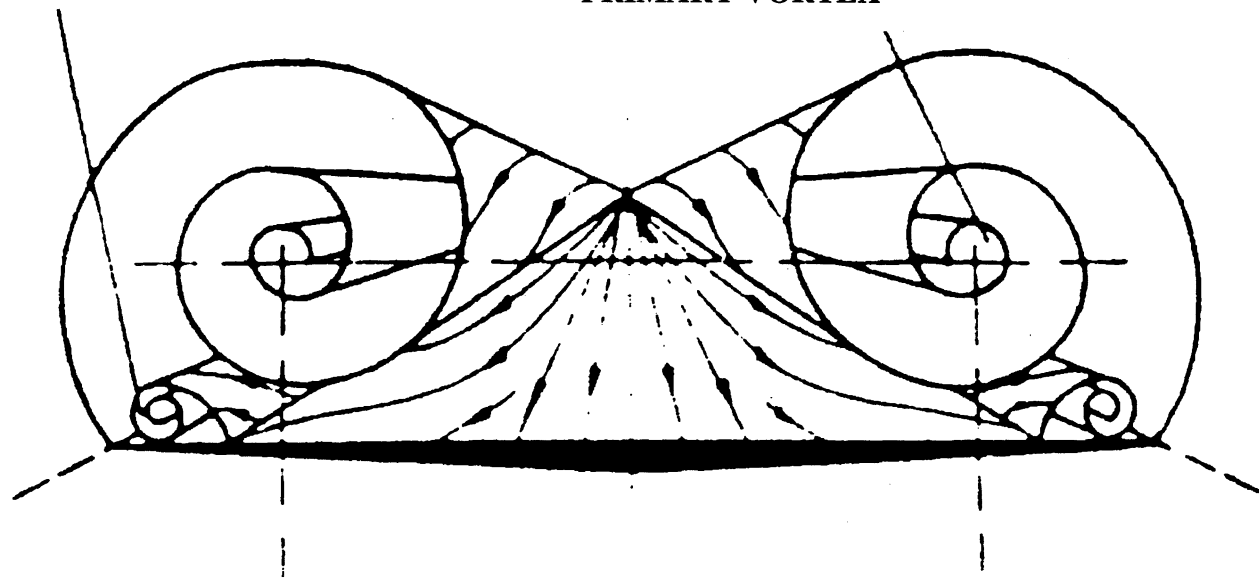


Figure 1.6 - Cross section of primary and secondary vortices for flow over a delta wing[13].

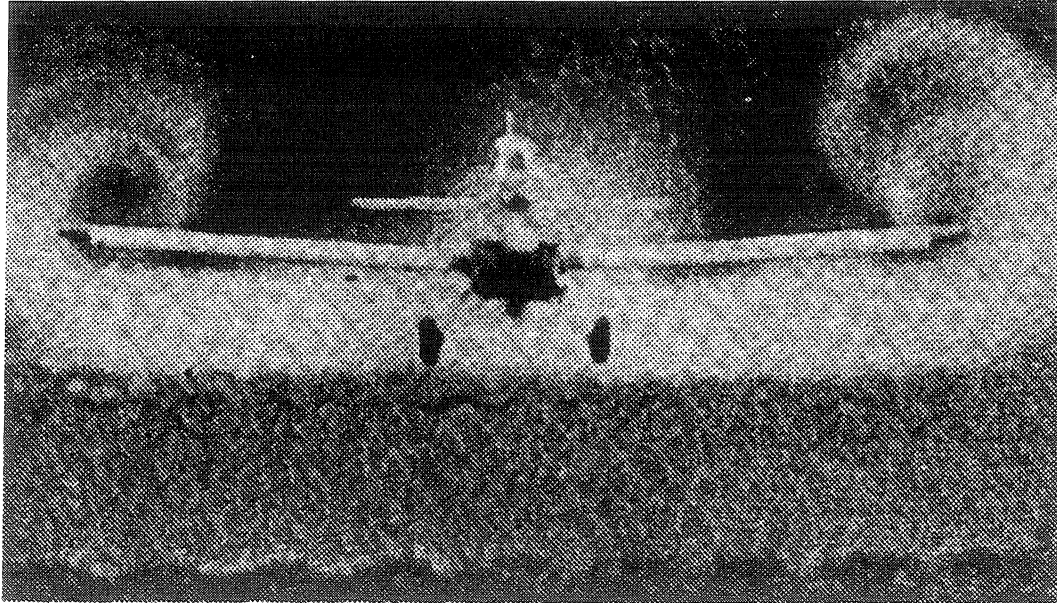


Figure 1.7 - Frontal view of trailing vortices from an aircraft wing[10].

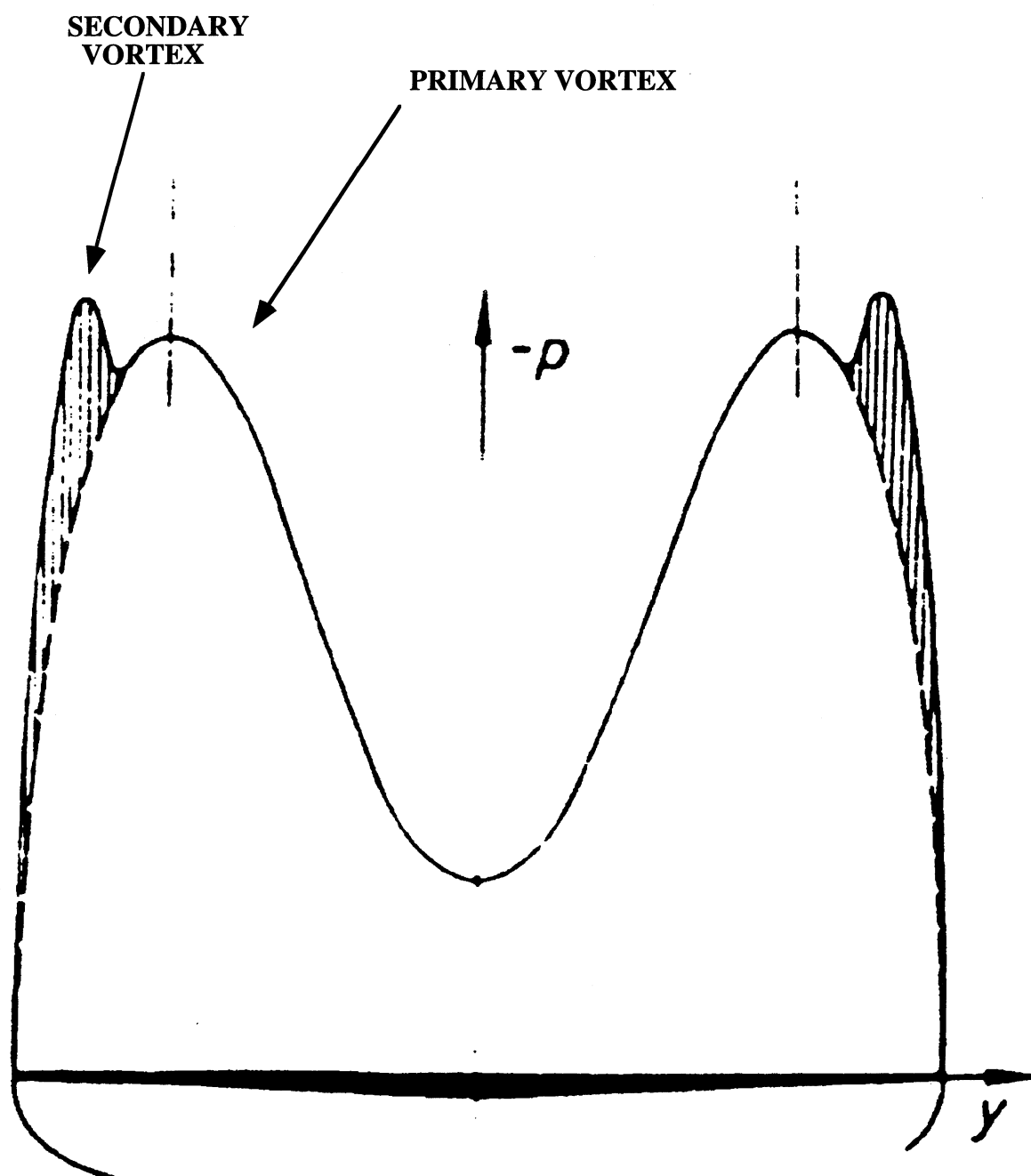


Figure 1.8 - Spanwise lift distribution across a delta wing resulting from the primary and secondary vortices[13].

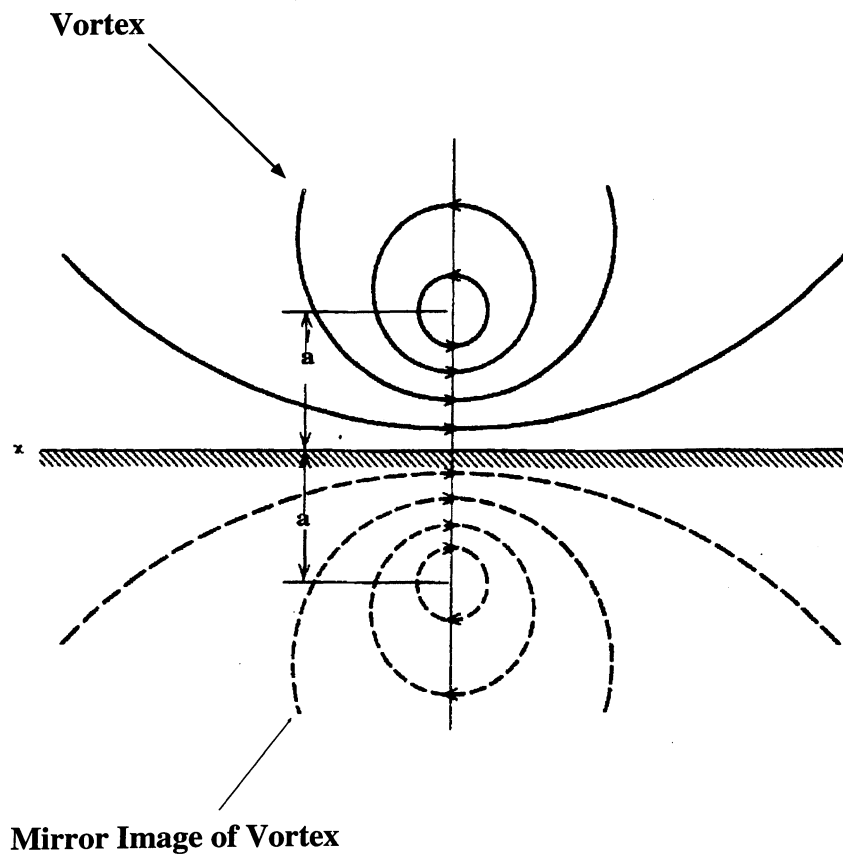


Figure 1.9 - Mirror image of a typical vortex interacting with a flat wall[12].

Chapter 2 - Experimental Methods and Facilities

The experimental investigation was performed with a test model that consisted of a series of parallel plates mounted in the test section of a low-speed wind tunnel (figures 2.1 and 2.2). The parallel plates represented test fins of a prototype plate heat exchanger with a vortex generator fixed to the leading edge of the center test fin (figure 2.3). For the heat transfer portion of the experiment, a vortex generator was only fixed to the center plate to prevent obstructing the view of the heat transfer surface. Local and average temperature values of the center test plate were measured using liquid crystal thermography and these data were used to determine the convective heat transfer coefficient. Pressure drop penalty data were measured using a pressure transmitter in conjunction with pressure taps mounted upstream and downstream of the test model. For the pressure drop penalty measurements, delta wings were fixed to all of the plates in the prototype heat exchanger.

2.1 Wind Tunnel and Test Section

2.1.1 Wind Tunnel - A schematic of the wind tunnel system is shown in figure 2.1. Air was drawn through the inlet, the honeycomb flow straightener, and a series of screens. The flow passed through a 9:1 area contraction and into the test section. Downstream of the test section, the flow passed through the fan, an acoustic diffuser, a mass flow meter, and then discharged outside of the laboratory.

The contraction and flow straightener were designed to ensure a flat, low free stream turbulence velocity profile. Using a hot-wire anemometer, the measured degree of turbulence was between .95% and 1.25% for the test-section velocity range of this experiment (.68 to 2.58 m/s) and a maximum velocity nonuniformity of 3.16% was recorded for the approach velocity profile (figure 2.4). Gentry[5] and DeJong[45] have presented a complete description of this wind tunnel system.

2.1.2 Test Section and Test Model - In order to obtain good optical access and low thermal conductivity, both the test section (15.24 x 15.24 x 91.44 cm) and prototype-plate heat exchanger (15.24 x 15.24 x 15.24 cm) (test model) were made of plexiglass. The test model consisted of five evenly spaced (2.41cm apart) parallel plates with the center plate used to measure the heat transfer coefficient (figure 2.2). All of the plates were .32 cm thick. A section of the center test plate was covered with a 25 μ m thick Nickel-alloy foil, and along the top and bottom edges were copper bus bars that provided power distribution for the foil heater (figure 2.3). Calculated results showed that the heat conduction losses through the plexiglass plate were 4.5 % to 10.3 % of the heater input power over the Re range tested. The heat transfer data were corrected for the conduction losses. Fixed to the leading edge of the center test fin was the delta-wing vortex generator at angle of attack to the main flow.

2.2 Instrumentation and Data Acquisition

For the heat transfer runs, the upstream air temperature, heater voltage and current, and pressure drop across the orifice plates were recorded. The air temperature was recorded using a calibrated RTD and a 12-bit A/D board. The power to the heater was provided by a Hewlett-Packard, 6269B power supply; voltage and current were measured using a hand held Fluke-27 multimeter. Pressure drop measurements across the orifice plate were accomplished using a Dwyer electronic manometer.

Pressure drop data across the core of the test model were measured using a pressure transmitter with a range of 0 to 24.9 Pa.

During the color-temperature calibration runs, upstream air temperature was recorded and the heater surface temperature was determined using T-type thermocouples and an A/D board. The wind tunnel was in the off mode during this phase of the experiments.

2.3 Heat Transfer, Pressure Drop Penalty and Velocity Measurements

2.3.1 Heat Transfer Measurements - The heat transfer results were obtained through a four-step process. First, the heater was coated with thermochromic liquid crystals (TLCs); second, a color-temperature lookup table was developed from the calibrated data; third, heat transfer experiments were performed; and lastly, the heat transfer data were reduced.

The heat-transfer surface was coated with TLCs using an air brush. For a vibrant display of the TLC colors, the surface was first coated with a black paint. In preparation for image recording, the TLC-coated heater surface was illuminated with a 150W Fiber-Lite, A-240P light source. A 35mm camera was stationed perpendicular to the heat transfer surface for recording the images; the camera was positioned 123.83 cm from the floor and 31.12 cm from the test section. The light source was at the same vertical position as the camera; its horizontal position was 52 cm from the test section and it was at a 45° angle to the heat transfer surface.

A color-temperature lookup table was developed by recording reference images of the heat transfer surface, and then scanning them to transform the images into a digital format. Thermocouples (attached to the unexposed side of the heater surface) were used to measure the surface temperature; the recorded temperature range for this TLC was 30.2 to 35.8° C. The digitized data of the reference images and the surface temperature data were used to complete the development of the color-temperature lookup table. For each entry in the color-temperature table the following information was stored: color table position, surface temperature, and digitized data describing the color behavior (i.e. red, green, blue values); see appendices A and B for a complete description of the color-temperature lookup table and table A.1 for the color-temperature lookup table used in this study.

The heat transfer experiments were divided into two phases: unenhanced and enhanced heat transfer. Enhanced heat transfer experiments were performed with the delta wing vortex generator (VG) fixed to the leading edge, while the unenhanced heat transfer experiments were performed without the VG. Images were recorded of the unenhanced heat transfer surface at predetermined velocity values. The enhanced heat transfer runs immediately followed the unenhanced heat transfer experiments. A delta-wing vortex generator was fixed to the leading edge of the center plate and set at an angle of attack to the main flow. Images were recorded of the enhanced heat transfer surface for the same velocity values as the unenhanced heat transfer experiments. Before each test (enhanced and unenhanced runs), the upstream air temperature was measured with an RTD and the heater voltage and current data were measured with a hand-held voltage-ohm meter.

After the heat transfer experiments were completed, the film negatives were developed and the negatives were scanned to transform the images into a digital format. Employing the color-temperature lookup table and *Image* software, the local and average surface temperature values were determined.

In order to reduce variability of the recorded and scanned images, the following steps were taken:

- a. Images for the color-temperature lookup table and heat transfer experiments were recorded using film that had the same lot number.
- b. Film was refrigerated until the calibration and heat transfer experiments began.
- c. The same film processing method was used for developing the images for calibration and heat transfer runs.
- d. Images were recorded with the same camera; the camera position and light source were in same position for the color-temperature calibration and heat transfer experiments.
- e. Only film negatives were used for transforming the images to a digital format.

2.3.2 Pressure Drop Penalty Measurements - Pressure taps were located upstream and downstream of the test model. The pressure drop across the core of the test model was measured using a pressure transmitter with a range of 0 to 24.9 Pa. Pressure drop data were recorded for conditions with and without vortex generators mounted to the leading edge of the plates. For the configuration with vortex generators, a delta wing was fixed to the leading edge of each plate in the test model. These data were used to determine the pressure drop penalty associated with applying vortex generators in channel flows for heat transfer enhancement.

2.3.3 Test Section Velocity Measurements - Flow in the test section was measured using an orifice plate, placed in a 10.16 cm diameter pipe. The bore diameter of the orifice plate used for this experiment was 7.62 cm. Four pressure taps were located one pipe diameter upstream and four pressure taps were located one-half diameter downstream of the orifice plate. The pressure taps were positioned in 90° intervals around the circumference of the 10.16 cm diameter pipe. The pressure drop across the orifice plate was measured using an electronic manometer, and these data were used to determine the test section velocity. Gentry[5] and DeJong[45] have provided a complete description of the orifice plates, and additional information is available in appendix C for calculating the test section velocity.

Data for the heat transfer and pressure drop experiments were reduced and represented using the Fanning friction factor, Reynolds number, and the Nusselt number; see appendix C for data reduction procedure and uncertainty analysis, and appendix D for derivation of the key equations.

2.4 Digitizing Equipment

The heat transfer and calibration images were transformed into a digital format using a 24-bit Leafscan-45 scanner, Power Macintosh 8100/110 computer, and *Photoshop* software. The Leafscan-45 scanner is a charge couple device (CCD) camera for digitizing color or black and white film, and has a resolution capability up to 5000 dots

per inch (dpi) . It can be used to scan positive transparencies or negative film and can produce either color or black and white output. For this study, all of the images were digitized using negative film, and the digitized resolution was 800 dpi. Once the images were scanned, the digitized data were stored on the computer (figure 2.5).

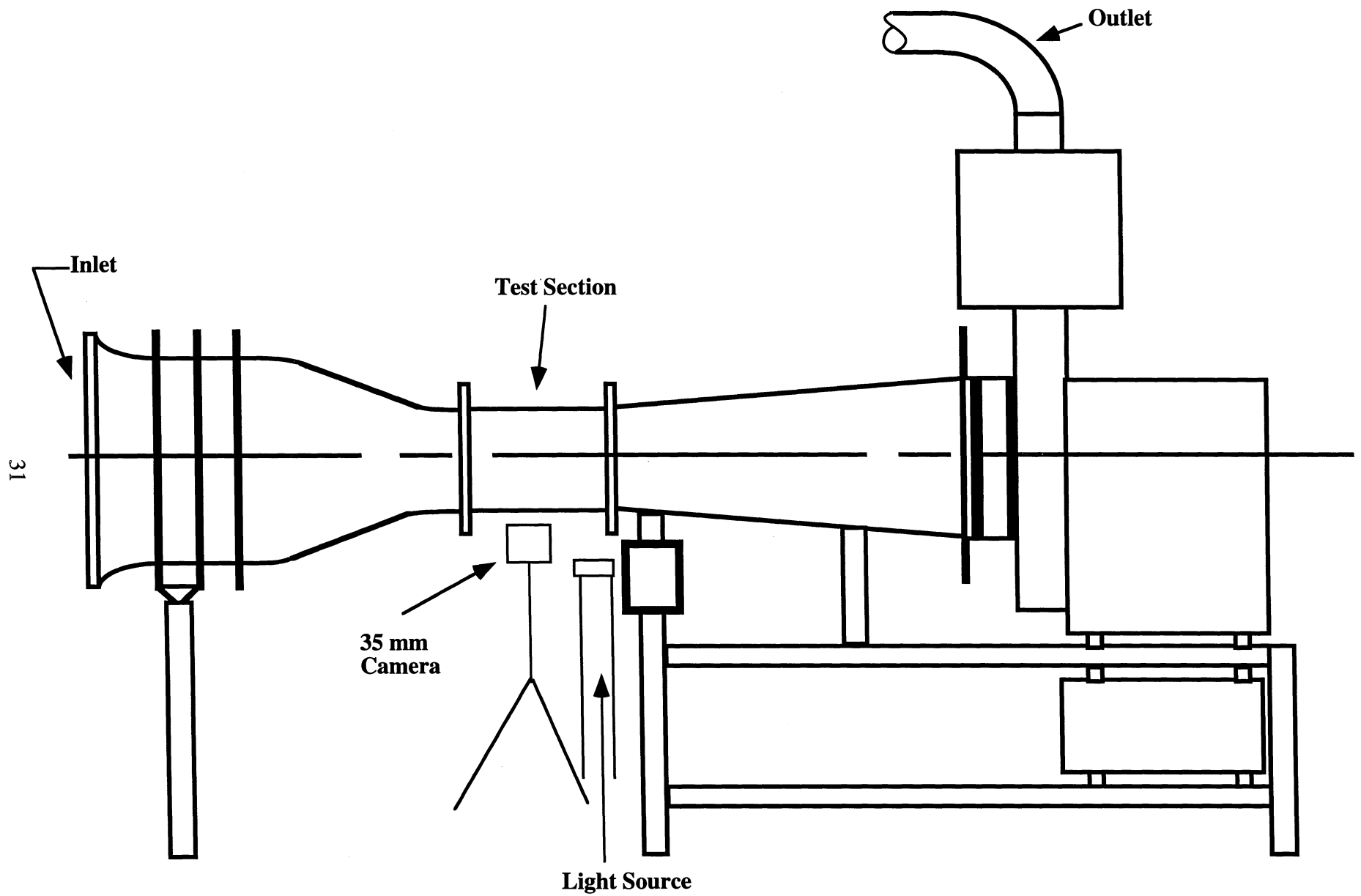


Figure 2.1 - Sketch of wind tunnel used in this study.

**Frontal View of Prototype
Plate Heat Exchanger**

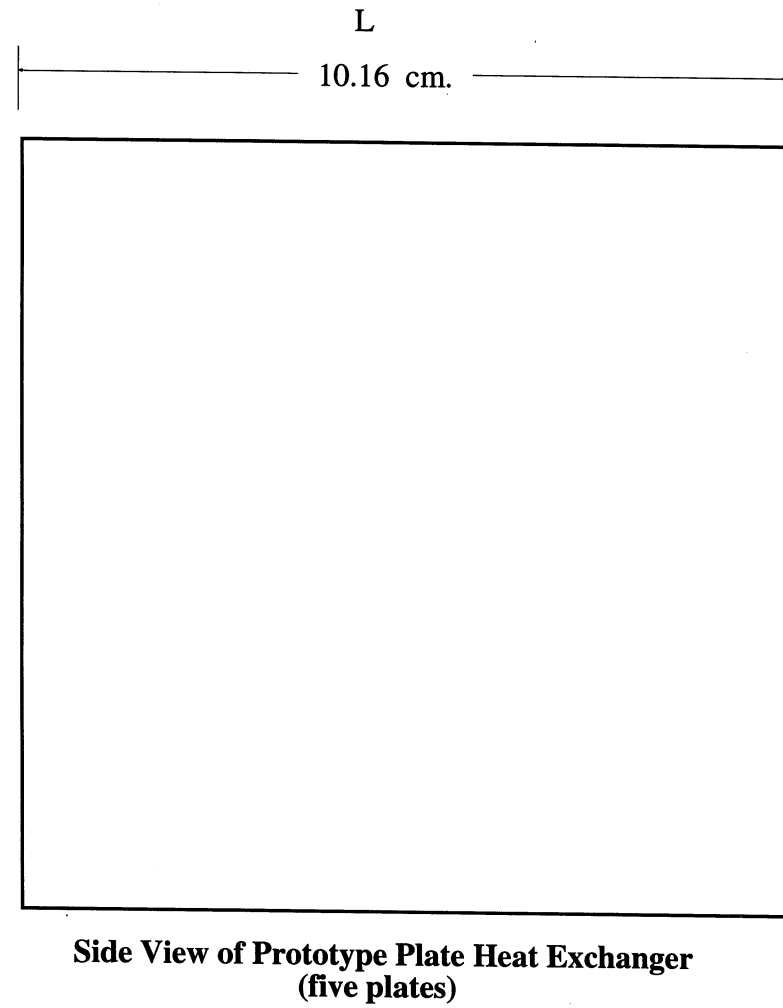
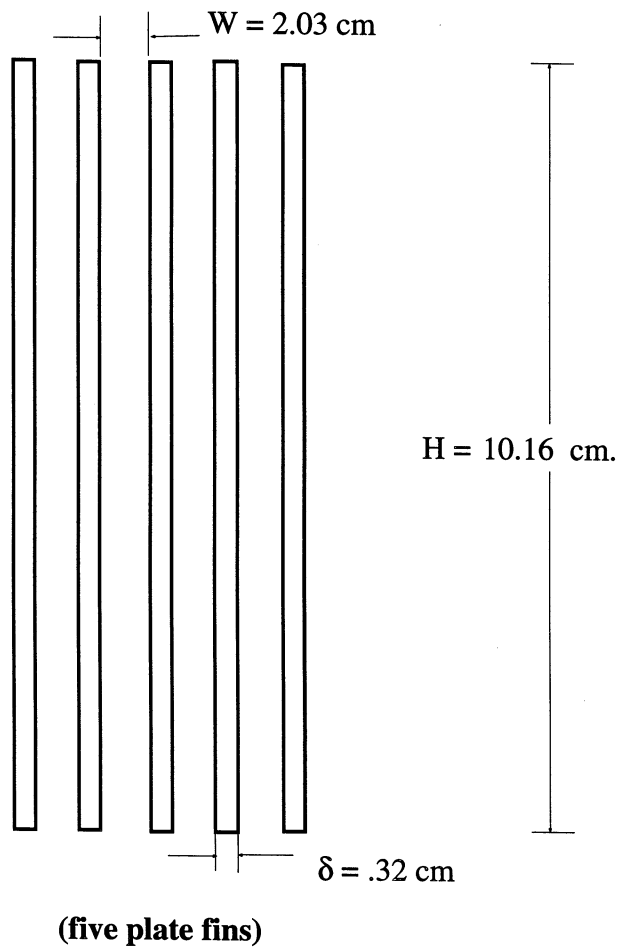


Figure 2.2 - Sketch of prototype heat exchanger used in this study.

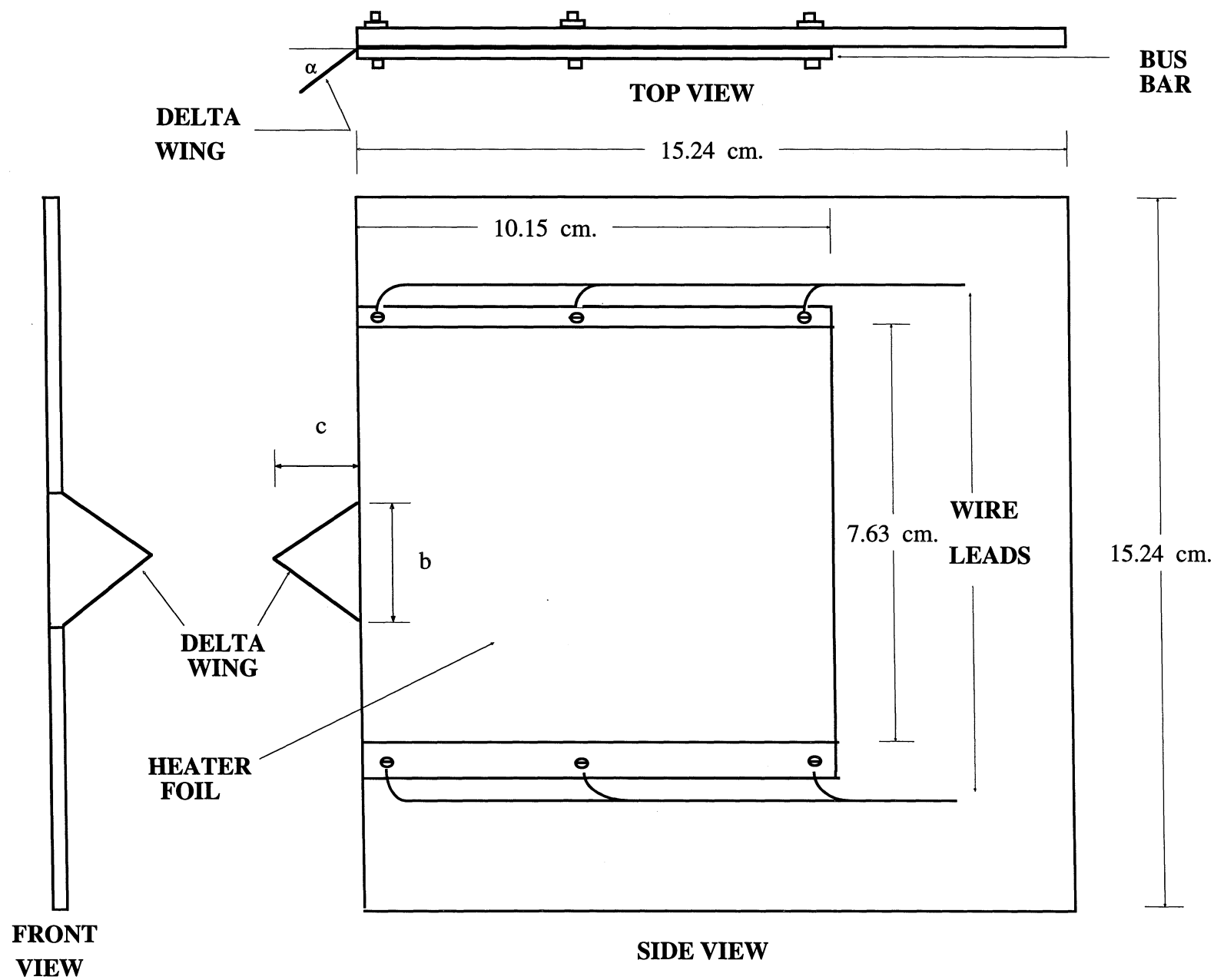


Figure 2.3 - Sketch of center test fin used in this study.

Mean Test Section Velocity vs Position

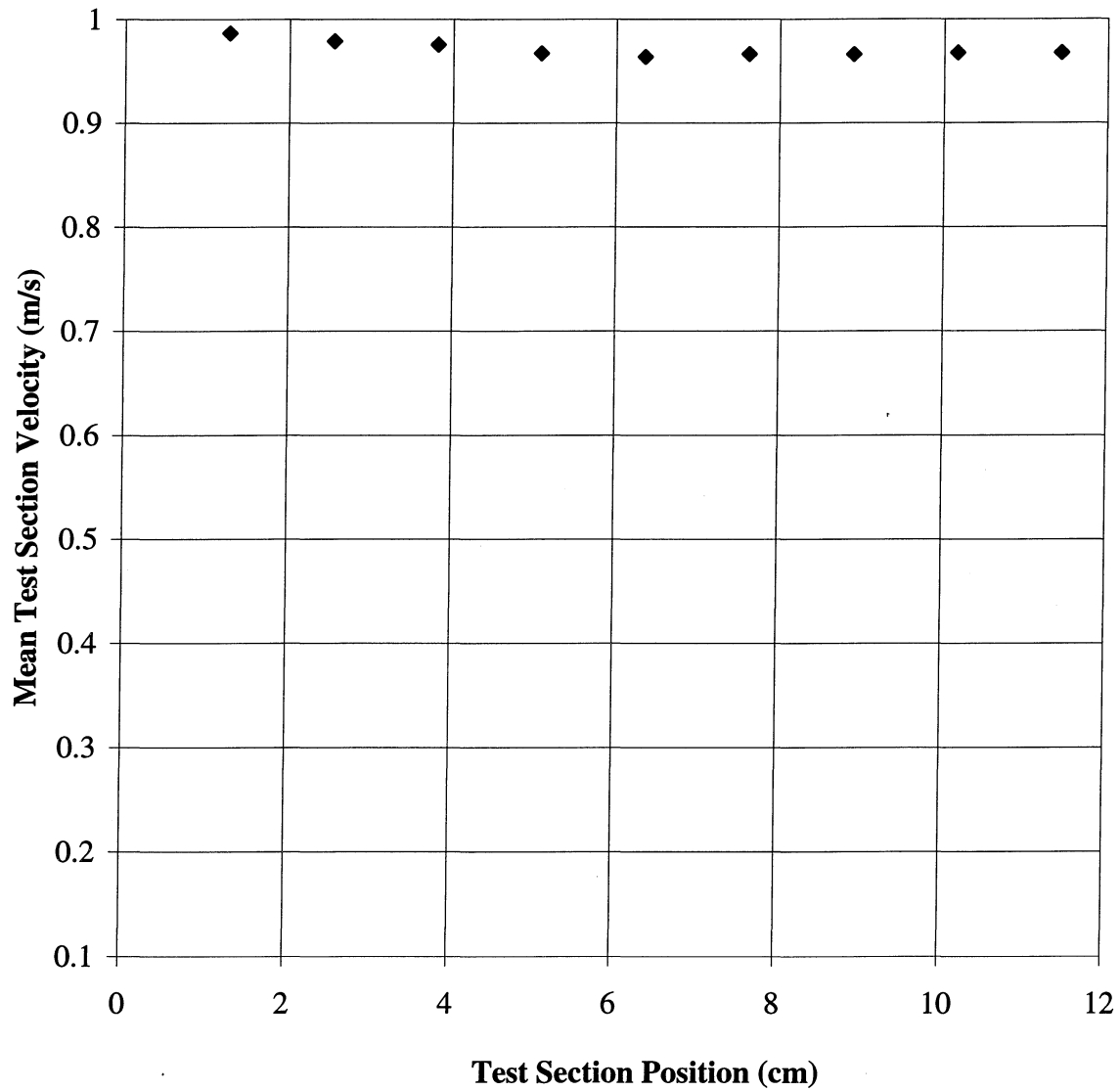


Figure 2.4 - Plot of mean test section velocity versus test section position.

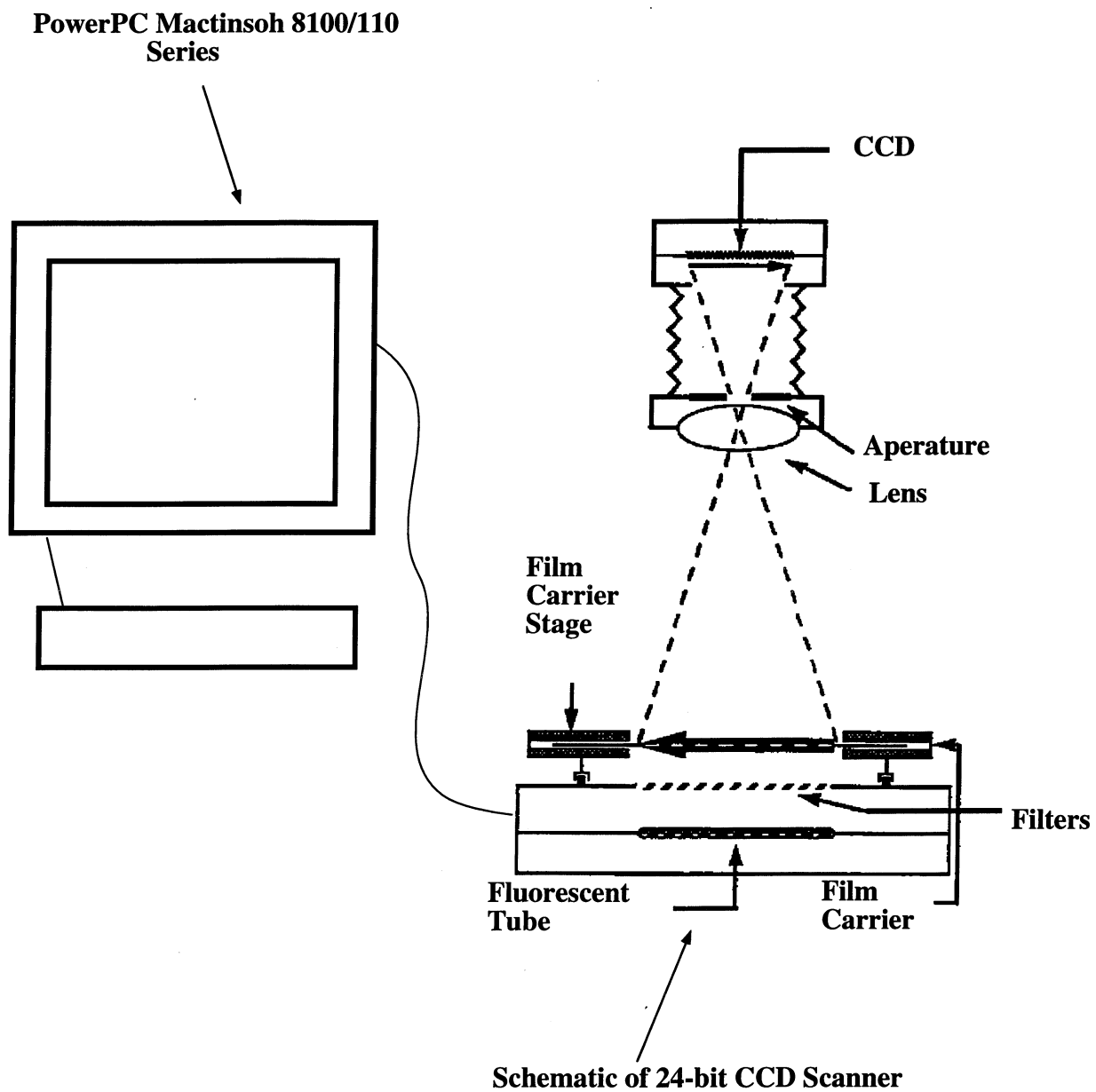


Figure 2.5 - Schematic of computer and digitizing equipment used to digitize 35 mm color negatives.

Chapter 3 - Results and Discussion

The heat transfer experiments were performed with a prototype heat exchanger, and a single delta wing vortex generator at the leading edge of the center test fin (figures 2.2 and 2.3). A vortex generator was only mounted on the center test fin because mounting vortex generators on the other plates would have obstructed the view of the surface coated with thermochromic liquid crystals. This obstruction would have prevented the recording of a full-field temperature map. In this chapter, the results from these experiments will be presented in the following order: liquid crystal thermography results, average heat transfer enhancement, local heat transfer enhancement, local temperature profiles and pressure drop penalty.

3.1 Liquid Crystal Thermography

For the color-temperature relation, images of the heat transfer surface (center test fin) were recorded for the full temperature band (30.2 - 35.8°C) of the thermochromic crystal liquid using a 35mm camera with a telephoto lens. The temperature-color relation was reduced by digitizing the heat-transfer surface images and developing a color-temperature table. Thirty-three images were recorded to produce the color-temperature table. In order to determine the color-temperature relation, it was necessary to specify and measure color, and this effort was achieved by using a standard color model.

In figure 3.1, the results of the color-temperature table demonstrate the effectiveness of color-temperature table approach. The RGB vector for color was converted into an integer value, and this integer value represented the color table position. There were 256 positions available in the color table; however, only 33 positions were used. Each position represented a calibrated color-temperature value. For example, position 1 was for white, position 2 was for red, position 255 was for blue, and position 256 was for black. Once the reference images were scanned, they were assigned a position in the table, and that position was assigned to the corresponding calibrated temperature. The

results plotted in figure 3.1 demonstrate that all of the rescanned images were assigned the correct color temperature position except for four values. In one case, the image in the incorrect color table position was .2° C high (color table position 49) and in another case it was .2° C low (color table position 67). The key to the repeatability of this method was using the same lighting condition and camera position for all of the experiments.

3.2 Summary of Experimental Conditions

Two aspect-ratio delta wing geometries were investigated in this study. Table 3.1 provides a summary of the conditions tested, and appendix E provides a discussion regarding the selection of the vortex generator geometries. As stated earlier, vortex generators (VG) were fixed to the leading edge of the heat exchanger plates. The VGs (for the enhanced heat transfer condition) were at an angle of attack to the main flow, resulting in blockage for a portion of the channel flow. This blockage resulted in a slightly different mean channel flow velocity than the unenhanced heat transfer condition; however, this effect was neglected. The Reynolds numbers given in table 3.1 correspond to face velocities of 0.7, 1.2, 2.0, and 2.6 m/s, respectively.

Table 3.1 - Summary of Delta-Wing Geometry and Experimental Conditions

<i>Aspect Ratio (Λ)</i>	<i>Reynolds Number (Re)</i>	<i>Alpha (α)</i>
2.0	1700, 2800, 5200, 6300	20, 30, 45 Deg
4.0	1700, 2800, 5200, 6300	20, 30, 45 Deg

3.3 Average Heat Transfer Enhancement

The average heat transfer enhancement data were experimentally determined for (aspect ratio) $\Lambda = 2.0$ and 4.0. The area of the vortex generators and heat-transfer surface used for the heat transfer enhancement evaluation are listed below in table 3.2. The ratio of the

heat transfer surface area to the vortex generator surface area was over 30 for both delta wings geometries evaluated in this study. For the aspect ratio 2 and 4 delta wing geometries, the heat transfer area used in this study equated to 60% (46.5 cm²) and 100% (77.4 cm²) of the heater area, respectively. The heater area (A_{HTS}) was 77.4 cm².

Table 3.2 - Summary of Dimensions for Delta Wing to Heat Transfer Surface Area Ratio

Delta-Wing Base(cm)	Delta-Wing Chord (cm)	$A_{DW}(\text{cm}^2)$	Λ	A_{HTS}/A_{DW}
1.59	1.59	1.26	2.0	37
2.22	1.11	1.24	4.0	63

Nusselt number values were compared for channel flow conditions with and without vortex generators. Results for $\Lambda = 2.0$ indicate that the heat transfer enhancement increases with Re for a given angle of attack. This trend is related to an increase in lift associated with a higher velocity. As noted in chapter 1, lift is proportional to velocity squared as well as circulation. As circulation increases, one could expect an increase in heat transfer. The lift coefficient versus angle of attack plots in figures 3.2 and 3.3 indicate that the lift coefficient increases with angle of attack and aspect ratio. In other words, for the same angle of attack a higher aspect-ratio delta wing would produce a higher lift, and the same aspect ratio with a higher angle of attack would produce a higher lift.

As noted earlier, the circulation increases with lift. Higher circulation has the potential of leading to more thermal boundary layer thinning. Visser and Nelson[46] reported experimental results for delta wing circulation, and the results indicated that circulation increased with angle of attack and velocity. They noted a maximum circulation was achieved when the maximum lift coefficient (cl_{max}) was obtained. According to Visser and Nelson, the start of vortex breakdown occurred at an angle of attack when the wing

reached cl_{max} ; they also noted that circulation began to decrease after the angle of the wing was increased beyond the cl_{max} position.

For $\Lambda = 2.0$, a delta wing at an angle of attack of 30 degrees was the better heat transfer performer within the laminar and transition to turbulence range ($Re = 1700 - 6300$) studied. The maximum heat transfer enhancement for $\Lambda = 2.0$ was 87% for $Re = 5200$ and $\alpha = 30^\circ$ (see figure 3.4). At the lower end of the Re range (1700) a reduction of 20% was recorded for $\alpha = 20^\circ$.

For the aspect ratio of 4 ($\Lambda = 4.0$) delta wing and $Re = 5200$ and 6300, the average heat transfer enhancement followed the same trend as the $\Lambda = 2.0$ delta wing (figure 3.5). However, the heat transfer enhancement trends, for $Re = 1700$ and 2800, $\Lambda = 4.0$, were different from the aspect ratio 2 delta wing. The reason for this behavior is unclear. Similar to the aspect ratio 2 delta wing, the delta-wing angle of attack of 30 degrees ($\Lambda = 4.0$) was the condition for maximum heat transfer enhancement ($Nur = 2.03$).

Selection of the heat transfer surface area had a significant impact on heat transfer enhancement. As stated earlier, the surface area used for the $\Lambda = 2.0$ delta wing enhancement evaluation was three fifths of the heater area; this heat transfer surface area was equal to 37 times the VG area. For the higher aspect ratio delta wing ($\Lambda = 4$), the area used for the heat transfer enhancement evaluation equated to 63 times the VG area. The larger heat transfer area was chosen $\Lambda = 4.0$ delta wing because the vortex spreading covered a larger spanwise space than the lower aspect ratio delta wing. This coverage of a larger spanwise space was due to the higher aspect ratio and larger delta-wing base. The region where the boundary layer thinning was most effective was the area with highest local heat transfer enhancement, and this area represented approximately 40% of the heater surface area. If this area (representing 40% of the heater area) was used for evaluating the average heat transfer enhancement ($\Lambda = 4.0$ and $\alpha = 30^\circ$), the average enhancement would have been 130 % and 120 % for $Re = 5200$ and 6300, respectively.

3.4 Local Heat Transfer Enhancement

Previous studies of local heat transfer enhancement produced by vortex generators have shown that common in-flow pair vortices enhance heat transfer. As discussed in chapter 1, the common inflow vortices move apart as the vortices propagate in the streamwise direction. According to Pauley and Eaton[47], the spreading of the vortices on a flat plate is due to the vortices interacting with the mirror images on the heat transfer surface. A similar spreading occurs in a developing channel flow. The local temperature profiles (figures 3.6 - 3.9) and local heat transfer enhancement plots (figures 3.10 - 3.13) show the impact of the spreading and local boundary layer thinning. The heat transfer enhancement was highest in the regions where the vortices were most effective (i.e. greatest boundary layer thinning). The X^* values used in the local heat transfer enhancement plots (figures 3.10 - 3.13) are for selected positions in the streamwise position. For figures 3.10 - 3.13, the maximum value of X^* is located at 55% of the heater length (H_l). The variables used to represent the nondimensional spanwise and streamwise positions are defined as:

$$X^* = x/(D_h Pe) \quad (3.1)$$

$$Y^* = 2y/H_w \quad (3.2)$$

where x represents the streamwise position, D_h represents the hydraulic diameter, Pe represents the Peclet number, y represents the spanwise position, and H_w represents the heater width.

As discussed in chapter 1, a viscous flow with heat transfer results in the development of a thermal boundary along the walls. In this study, fully developed conditions were never achieved in the channel flow. The local heat transfer plots highlight the impact of the boundary thinning produced by the vortex generator.

In the region immediately downstream of the delta-wing vortex generator ($X^* = 0.0000678$ and $X^* = 0.0000565$), the local heat transfer enhancement is high between $Y^* = -0.2$ and 0.2 . For example, in figure 3.10 the heat transfer enhancement is over 100% for $X^* = 0.0000678$ and Y^* between -0.2 and $+0.2$. In contrast, the heat transfer enhancement decreases to 40% for the same X^* position and $Y^* = -0.5$. As the vortices move downstream of the delta-wing vortex generator, they spread and thin the boundary layer for a wider spanwise region; the result of this vortex spreading is noted in local heat transfer enhancement plots. Further downstream ($X^* = 0.000407$), the heat transfer enhancement occupies a larger spanwise space.

The vortex spreading is even more evident when the upstream local enhancement values at $Y^* = 0.0$ and 0.5 are compared to the same Y^* values further downstream. Table 3.3 summarizes the impact of the vortex spreading and the impact of the increased lift due to higher velocity and circulation.

Table 3.3 - Summary of Selected Local Approximate Enhancement Values

<i>Figure</i>	<i>Y*</i>	<i>X*</i>	Λ	<i>Re</i>	<i>Nur</i>
3.10	0.5	0.0000678	2.0	5200	1.4
3.10	0.0	0.0000678	2.0	5200	2.1
3.10	0.5	0.000407	2.0	5200	2.1
3.10	0.0	0.000407	2.0	5200	2.2
3.11	0.5	0.0000678	4.0	5200	2.0
3.11	0.5	0.000407	4.0	5200	2.8

Changing the angle of attack, Re , and aspect ratio also impacted the width of the thermal boundary layer thinning. Figures 3.12 and 3.13 show that the width of the boundary thinning increases with aspect ratio and air velocity. As noted earlier, this spreading of

the boundary layer thinning was due to stronger vortices interacting with their mirror images in a developing channel flow. When this boundary thinning is evaluated quantitatively, figure 3.11 shows that the local enhancement tends to increase in the streamwise direction. This increase is due to a slower rate of decay for the enhanced heat transfer than for unenhanced heat transfer conditions.

The local Nusselt number ratio (Nur) is greater than 1 for all of the spanwise space presented in figures 3.10 - 3.13. For a fixed Re , this phenomenon is related to the higher channel flow velocity in the region of the vortices. Fiebig et al.[22] have documented that delta-wings mounted at the leading edge of a channel flow create vortices, resulting in an higher axial flow velocity than the base flow velocity for the vortex region.

Another condition that is of importance for local heat transfer enhancement was the development of a secondary vortex at high Re and high delta-wing angle of attack. In figures 3.8 and 3.9, one can see the impact of the secondary vortex on the temperature profile. The results of the local and average heat transfer enhancement show a complex interaction between the vortices and heat transfer enhancement capabilities of vortex-generators.

3.5 Local Temperature Profile

Plots of the local temperature (figures 3.7 and 3.9), for the two aspect ratio delta wings studied, indicate that the lowest surface temperature occurs aft of the delta wing. As the fluid moves downstream, the impact of vortices created by the vortex generator can be observed visually. For the $\Lambda = 4.0$ delta wing, the impact of both primary and secondary vortices are shown in figures 3.8 and 3.9. Although the primary and secondary vortices are shown in figure 3.7 for the $\Lambda = 2.0$, they are less pronounced. From the local temperature plots for the $\Lambda = 4.0$ delta wing (figures 3.8 and 3.9), one can infer that the secondary vortices would have had a greater impact on boundary layer thinning if a larger heat transfer surface area was used for this study. However, the local temperature plots

indicate that the secondary vortices did lower the surface temperature in the regions affected by these vortices.

3.6 Pressure Drop Penalty

In the design of heat transfer augmentation techniques, knowledge of the friction characteristics is also an important consideration in evaluating the potential application of this technique. The friction characteristics of the prototype heat exchanger used in this study were determined by measuring the pressure drop across the heat exchanger with and without vortex generators. This core pressure drop was analyzed on a dimensionless basis using the Fanning friction factor (f). The results showed that the Fanning friction factor decreased with Re for conditions with and without vortex generators (figures 3.14 and 3.15). The ratio of f with and without the vortex generators (f_{ent}/f_o) increased with Re ; it reached a maximum of 45% and 52% for $\Lambda = 2.0$ and $\Lambda = 4.0$, respectively (figures 3.16 and 3.17).

The results plotted in figures 3.17 and 3.18 show that both delta wings produced comparable friction factor ratios. The comparable values of friction factor ratio were due to equal flow blockage caused by the vortex generators of approximately the same projected area; the projected area of the vortex generators differed by less 2%.

A summary of the pressure drop penalty and heat transfer enhancement data will be presented in chapter 4.

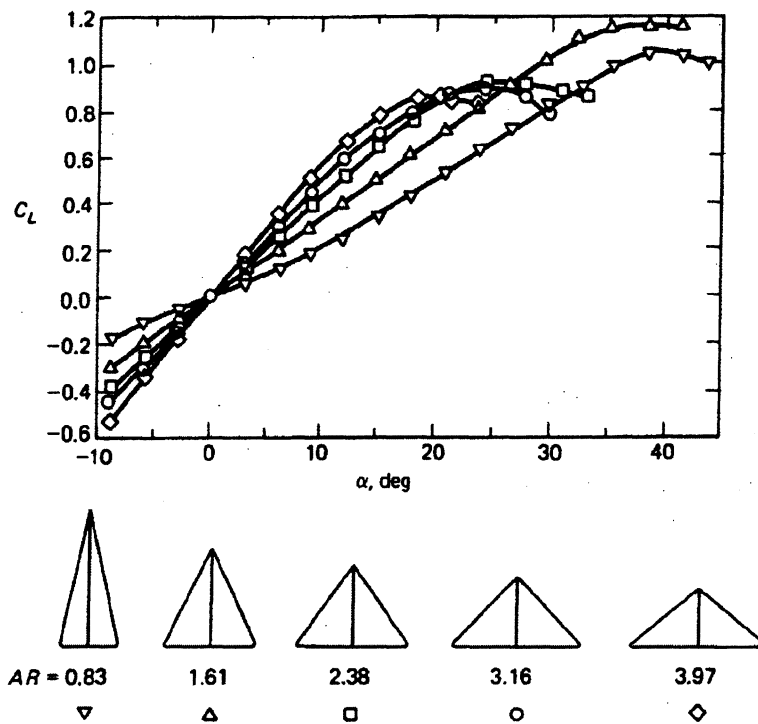


Figure 3.2 - Example of lift versus angle of attack for a delta wing in freestream velocity with an aspect-ratio range of .83 to 3.97[12].

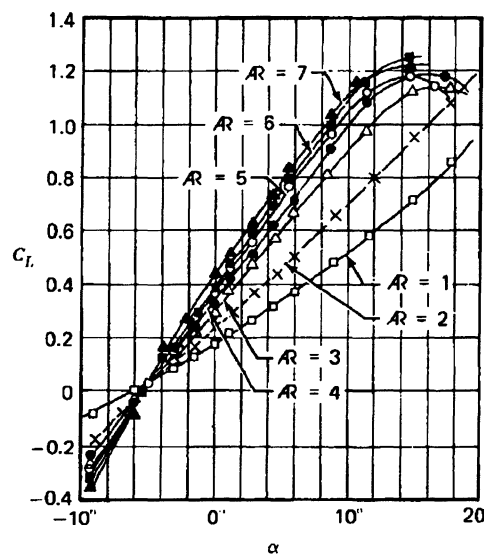


Figure 3.3 - Example of lift versus angle of attack for a rectangular wing in freestream velocity with an aspect-ratio range of 1.0 to 7.0[10].

Nusselt Number Ratio vs Angle of Attack

$\Lambda = 2.0$

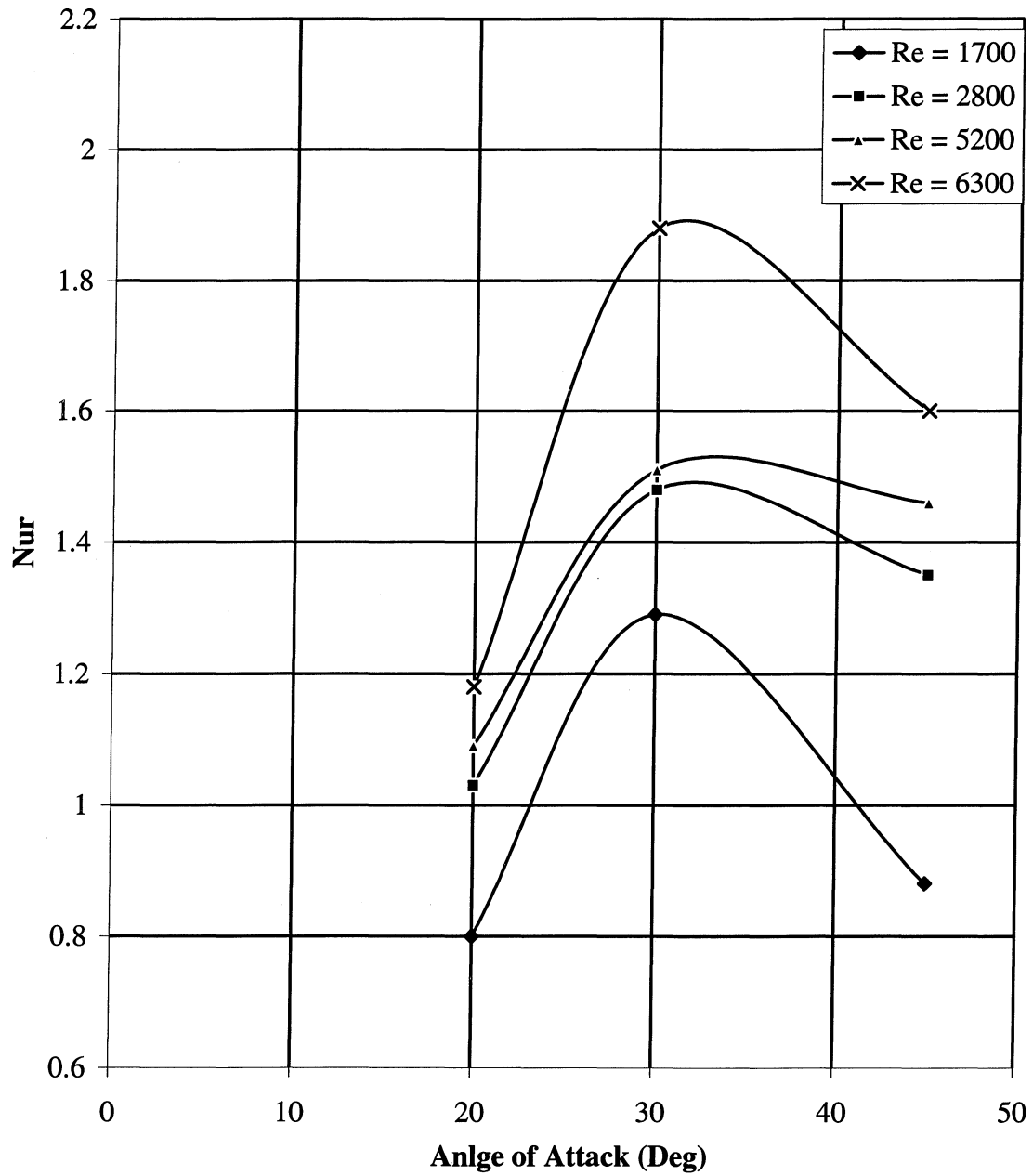


Figure 3.4 - Average Nusselt number ratio (enhanced to unenhanced) versus angle of attack for a delta-wing VG with an $\Lambda = 2.0$.

Nusselt Number Ratio vs Angle of Attack

$\Lambda = 4.0$

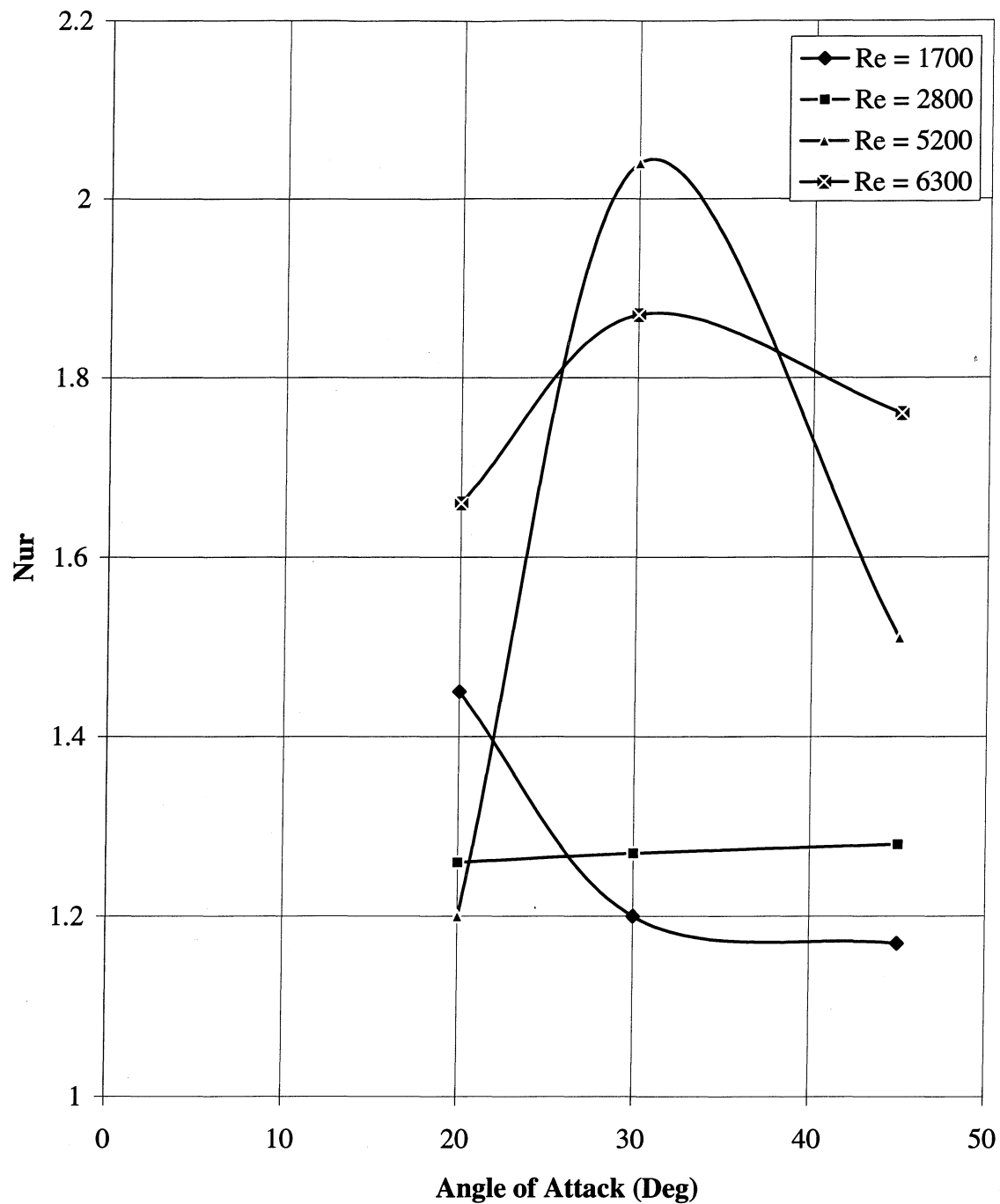
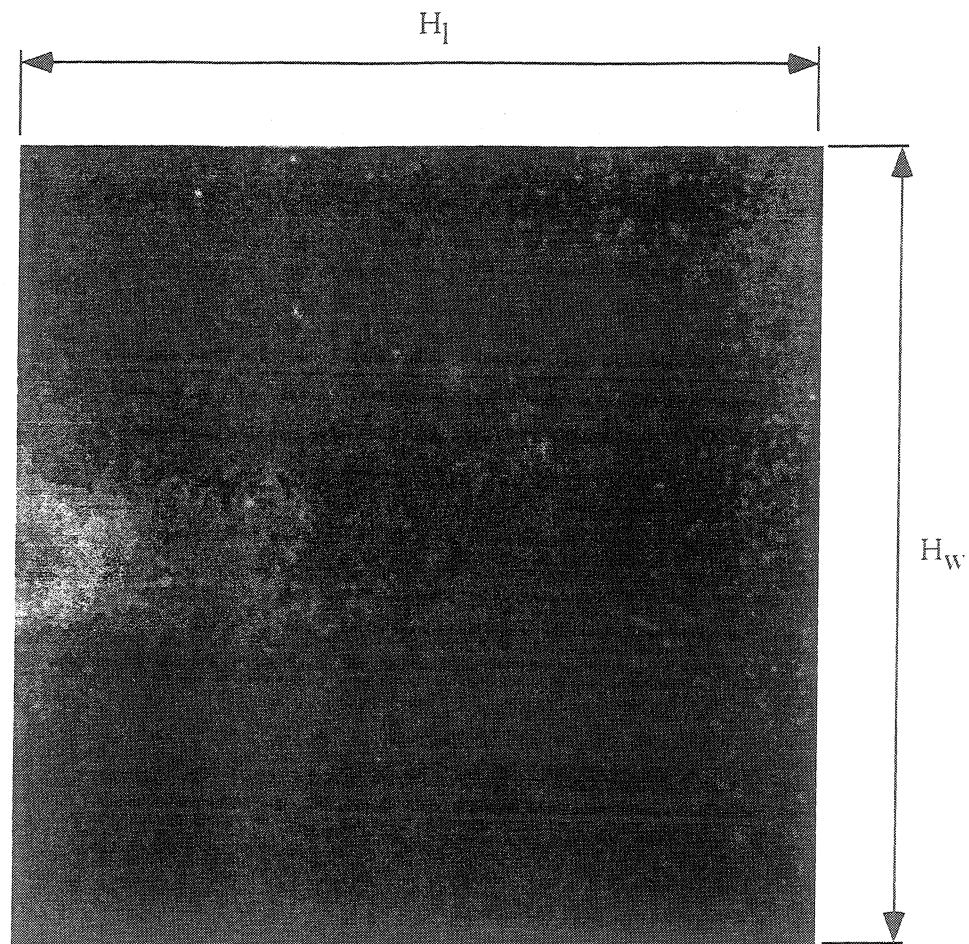
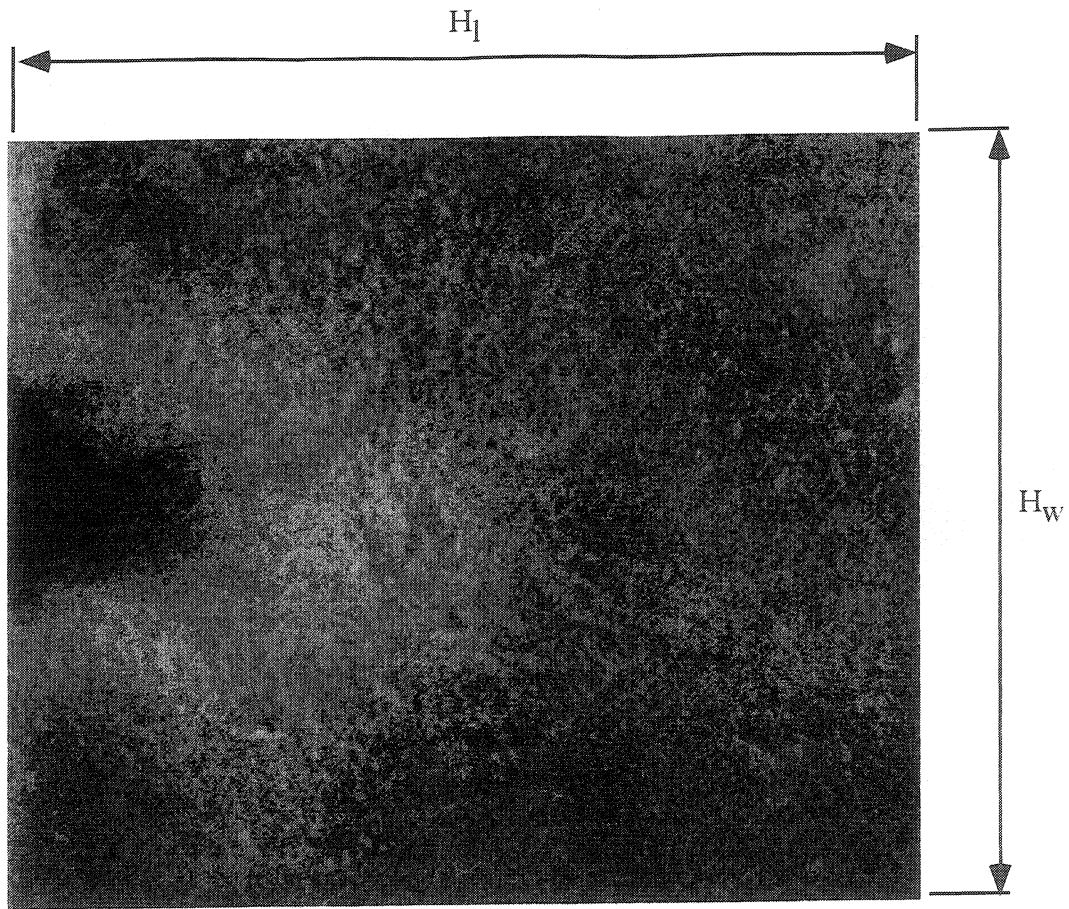


Figure 3.5 - Average Nusselt number ratio (enhanced to unenhanced) versus angle of attack for a delta-wing VG with an $\Lambda = 4.0$.



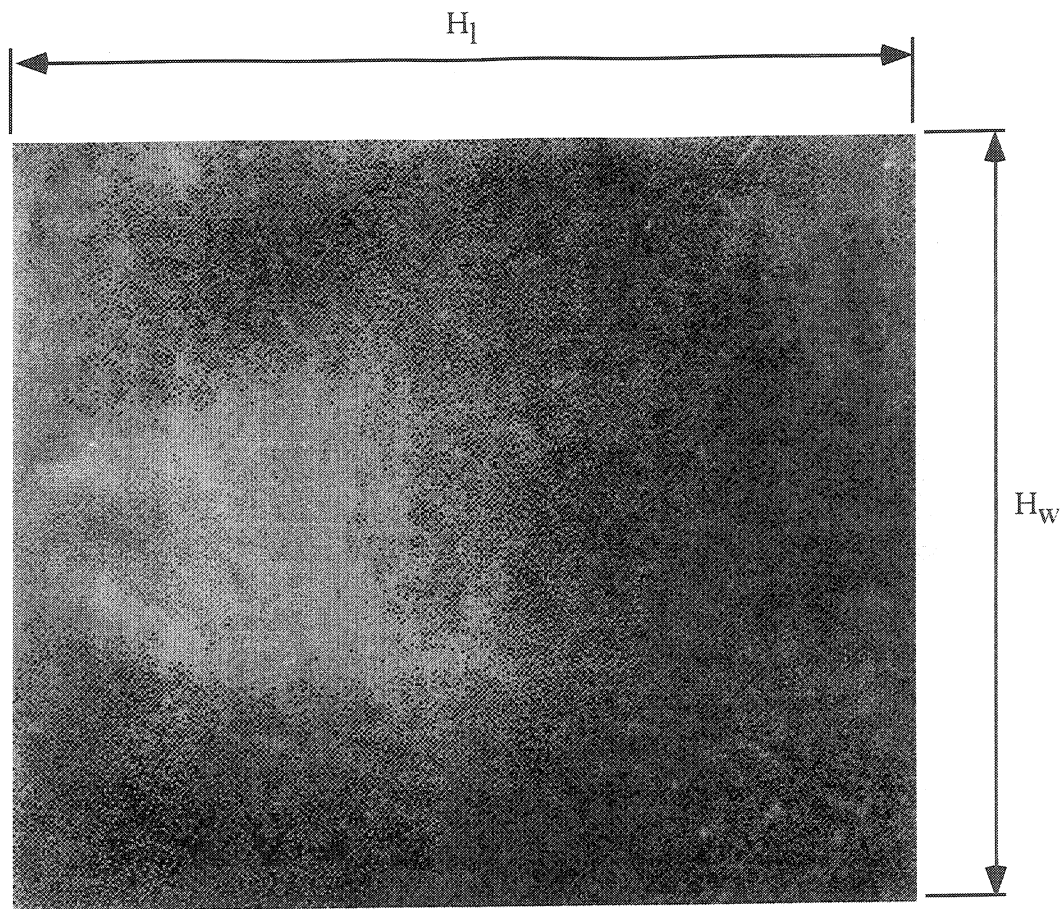
Color plates available upon request.

Figure 3.6 - Local temperature profile of heat transfer surface with a delta-wing vortex generator located at the leading edge (the left edge, with flow left to right). The delta wing configuration is: $\Lambda=2.0$, $\alpha=45$ deg., $Re=5200$. This gray-scale image represents the temperature distribution (black=35.8 C, white=30.2 C).



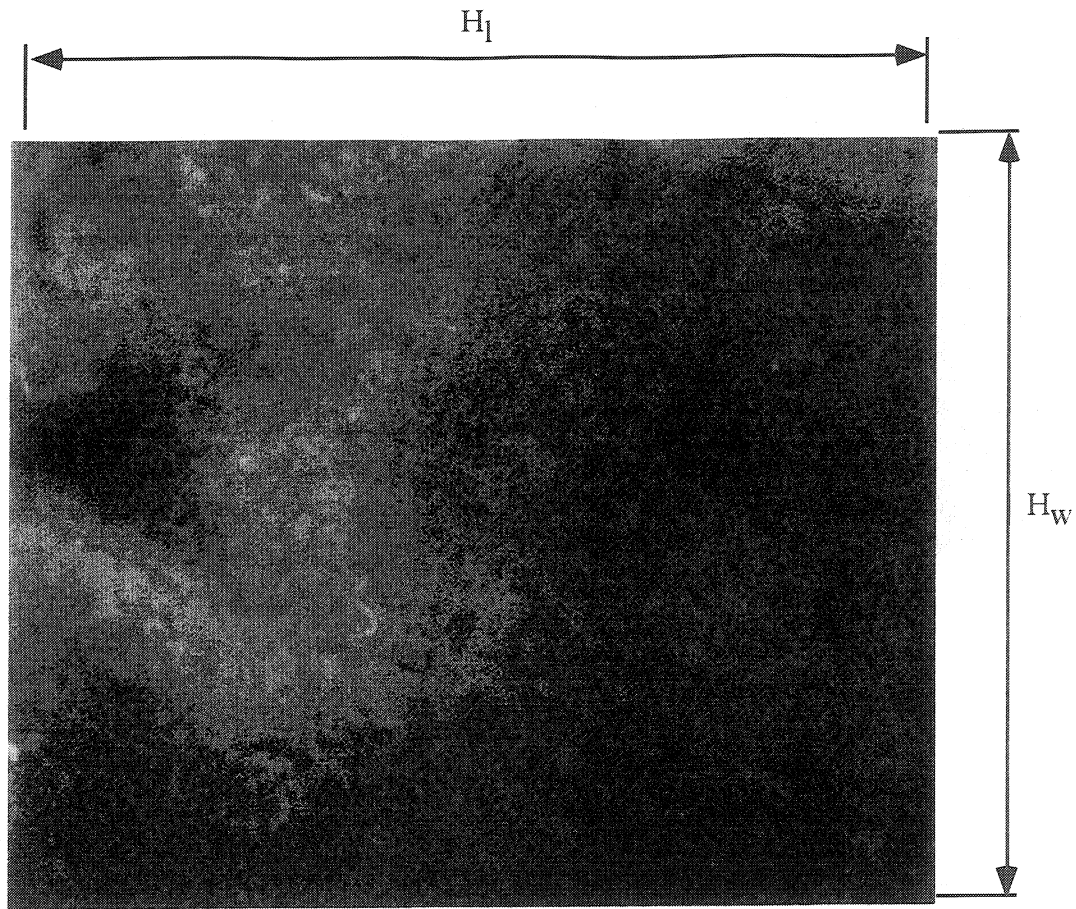
Color plates available upon request.

Figure 3.7 - Local temperature profile of heat transfer surface with a delta-wing vortex generator located at the leading edge (the left edge, with flow left to right). The delta wing configuration is: $\Lambda=2.0$, $\alpha=45$ deg., $Re=6300$. This gray-scale image represents the temperature distribution (black=35.8 C, white=30.2 C).



Color plates available upon request.

Figure 3.8 - Local temperature profile of heat transfer surface with a delta-wing vortex generator located at the leading edge (the left edge, with flow left to right). The delta wing configuration is: $\Lambda=4.0$, $\alpha=45$ deg., $Re=5200$. This gray-scale image represents the temperature distribution (black=35.8 C, white=30.2 C).



Color plates available upon request.

Figure 3.9 - Local temperature profile of heat transfer surface with a delta-wing vortex generator located at the leading edge (the left edge, with flow left to right). The delta wing configuration is: $\Lambda=4.0$, $\alpha=45$ deg., $Re=6300$. This gray-scale image represents the temperature distribution (black=35.8 C, white=30.2 C).

Local Heat Transfer Enhancement

$\Lambda = 2.0 \quad \alpha = 30 \text{ Deg} \quad Re = 5200$

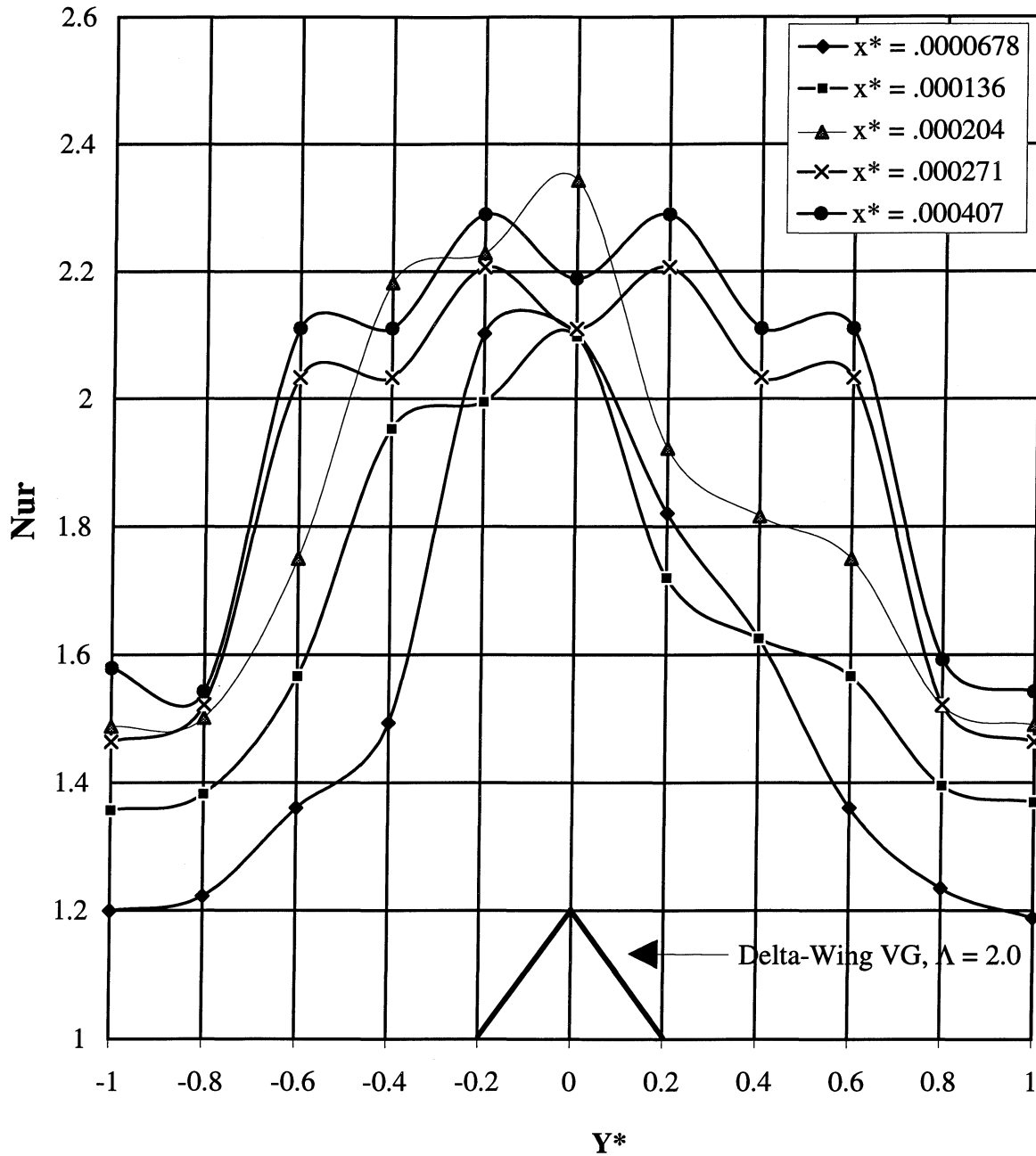


Figure 3.10 - Local spanwise heat transfer enhancement that was produced by a delta-wing VG; VG conditions were $\Lambda = 2.0$, $\alpha = 30$ degrees, $Re = 5200$.

Local Heat Transfer Enhancement

$\Lambda = 4.0$ $\alpha = 30$ Deg $Re = 5200$

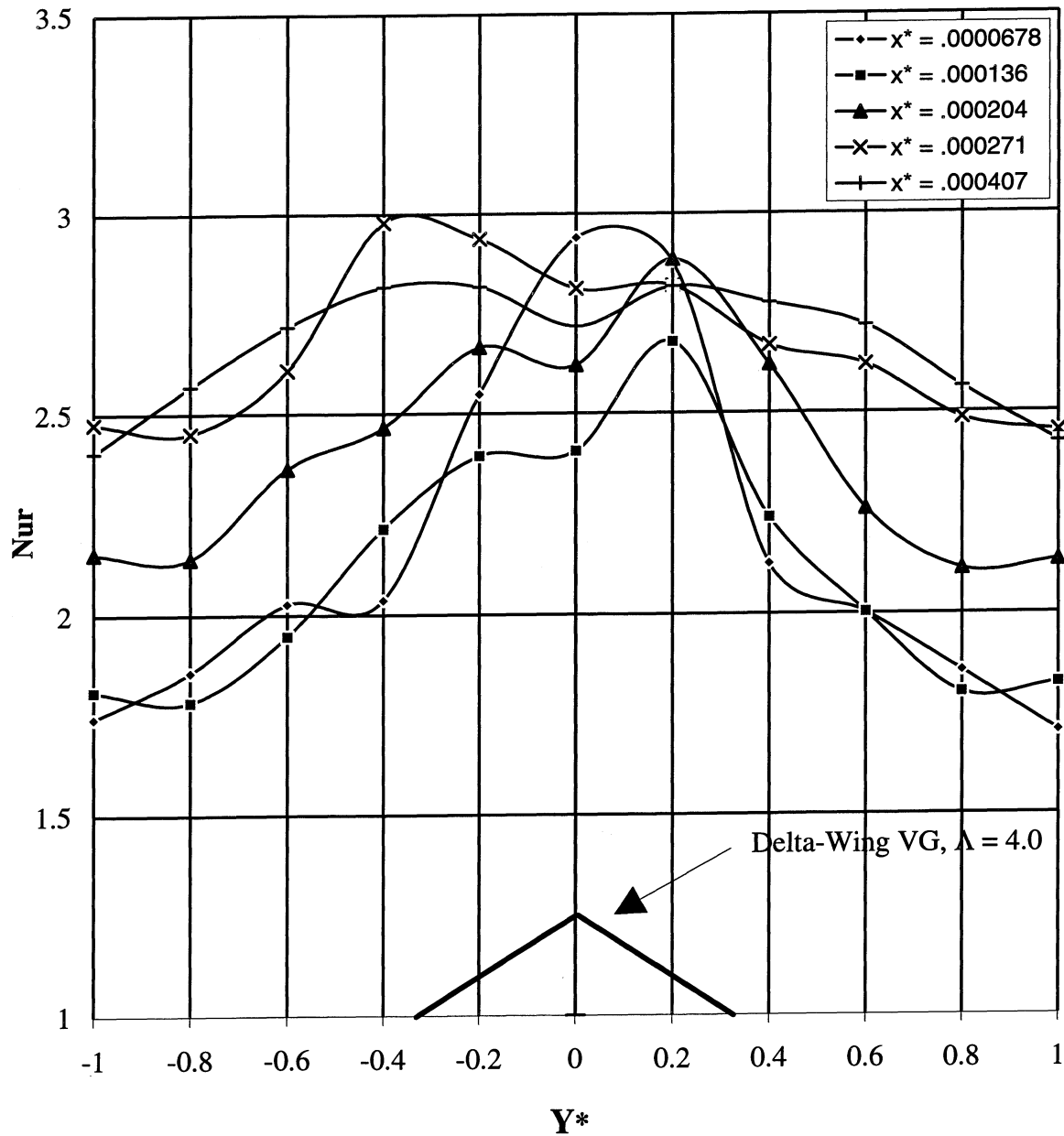


Figure 3.11 - Local spanwise heat transfer enhancement that was produced by a delta-wing VG; VG conditions were $\Lambda = 4.0$, $\alpha = 30$ degrees, $Re = 5200$.

Local HeatTransfer Enhancement

$\Lambda = 2.0$ $\alpha = 30$ Deg $Re = 6300$

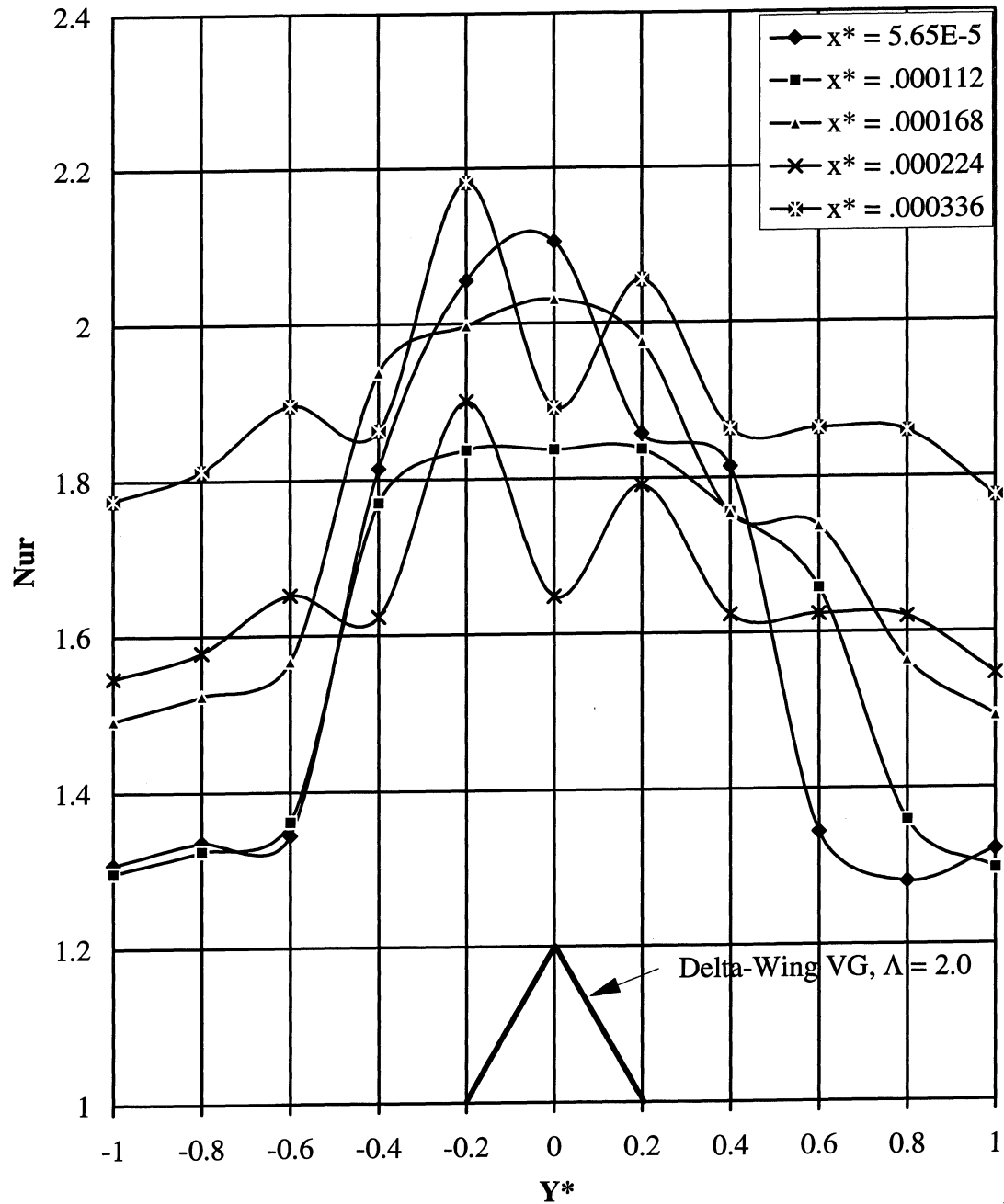


Figure 3.12 - Local spanwise heat transfer enhancement that was produced by a delta-wing VG; VG conditions were $\Lambda = 2.0$, $\alpha = 30$ degrees, $Re = 6300$.

Local Heat Transfer Enhancement

$\Lambda = 4.0$ $\alpha = 30$ Deg $Re = 6300$

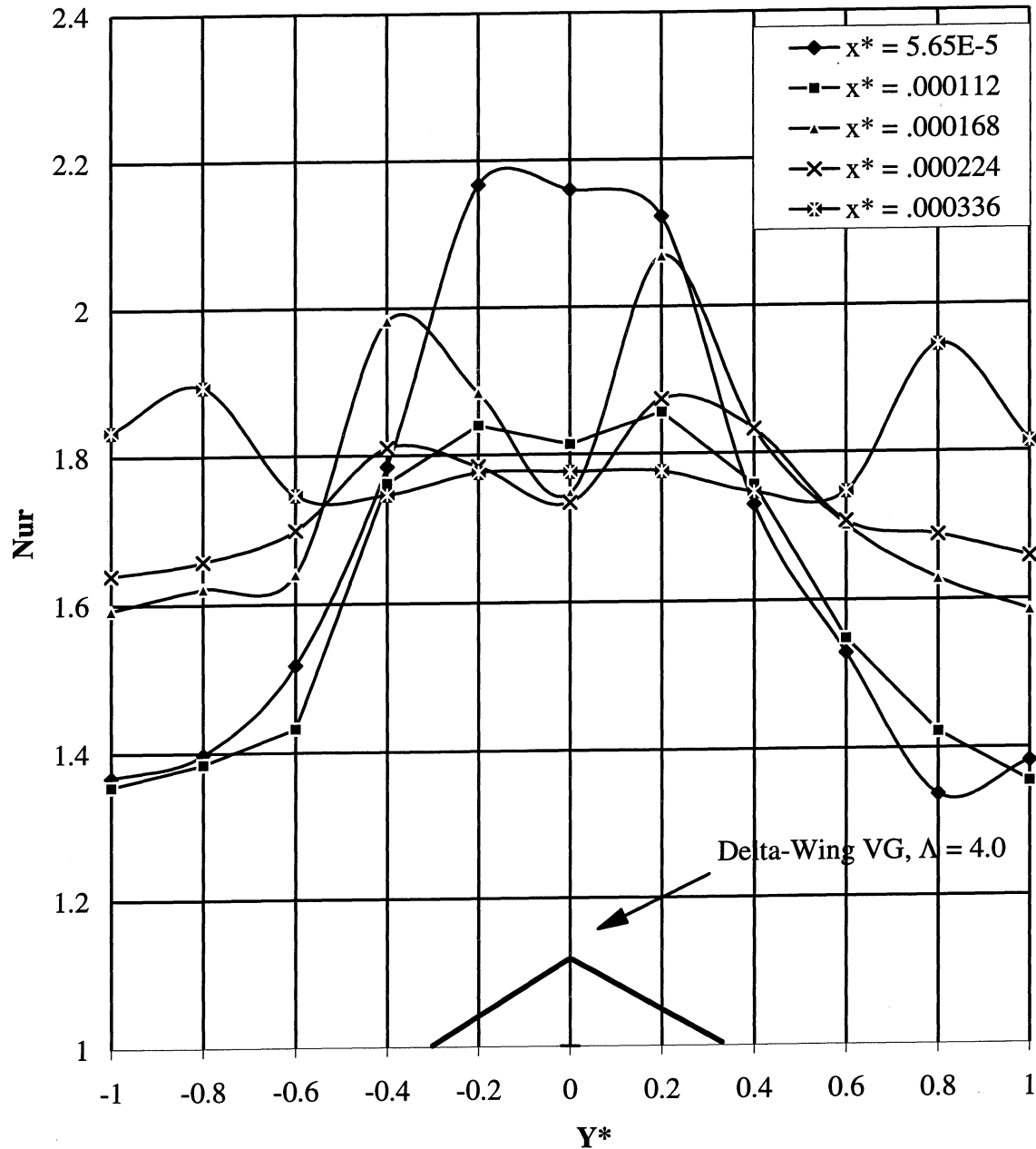


Figure 3.13 - Local spanwise heat transfer enhancement that was produced by a delta-wing VG; VG conditions were $\Lambda = 4.0$, $\alpha = 30$ degrees, $Re = 6300$.

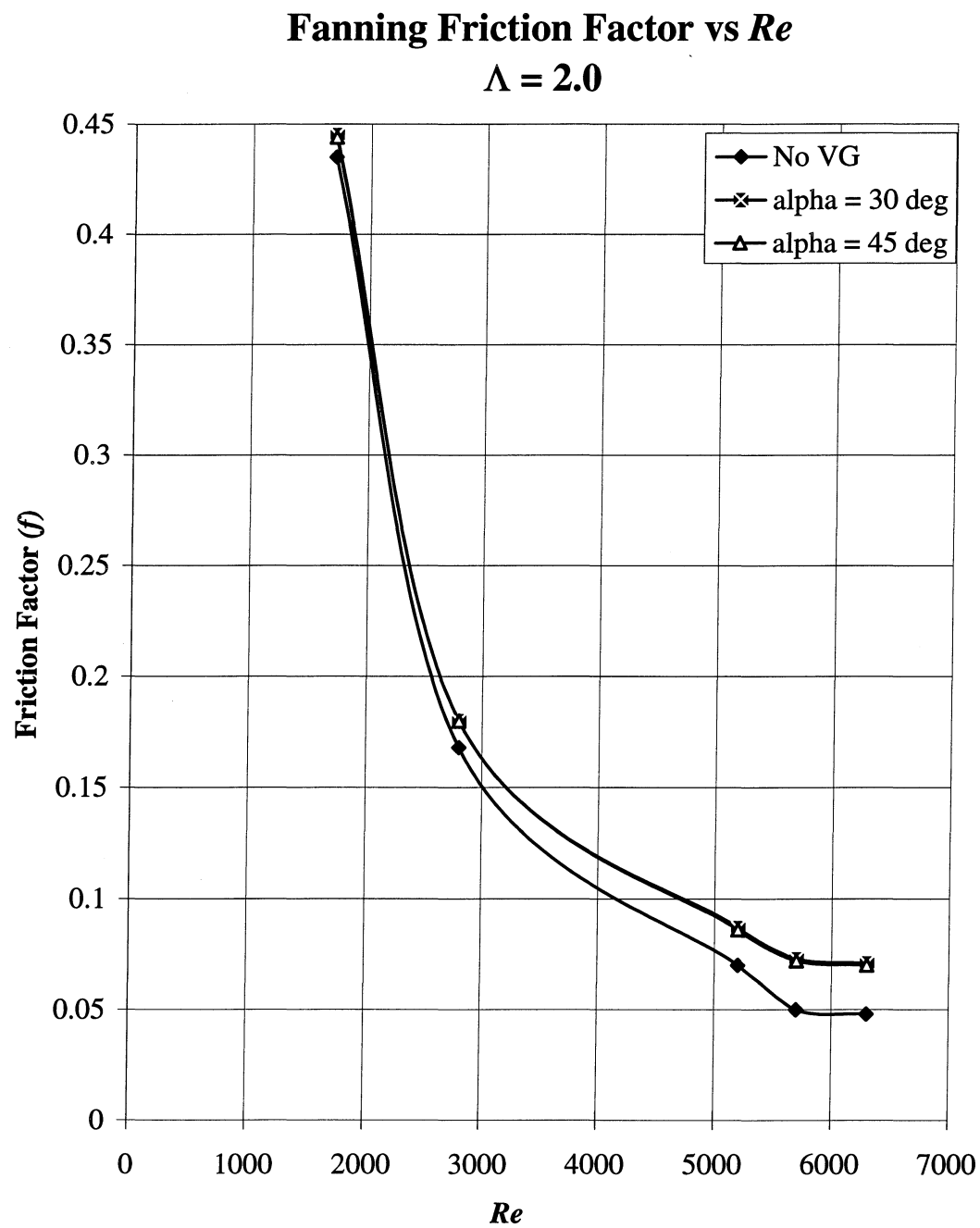


Figure 3.14 - Fanning friction factor versus Re for a delta-wing VG with an $\Lambda = 2.0$.

Fanning Friction Factor vs Re

$\Lambda = 4.0$

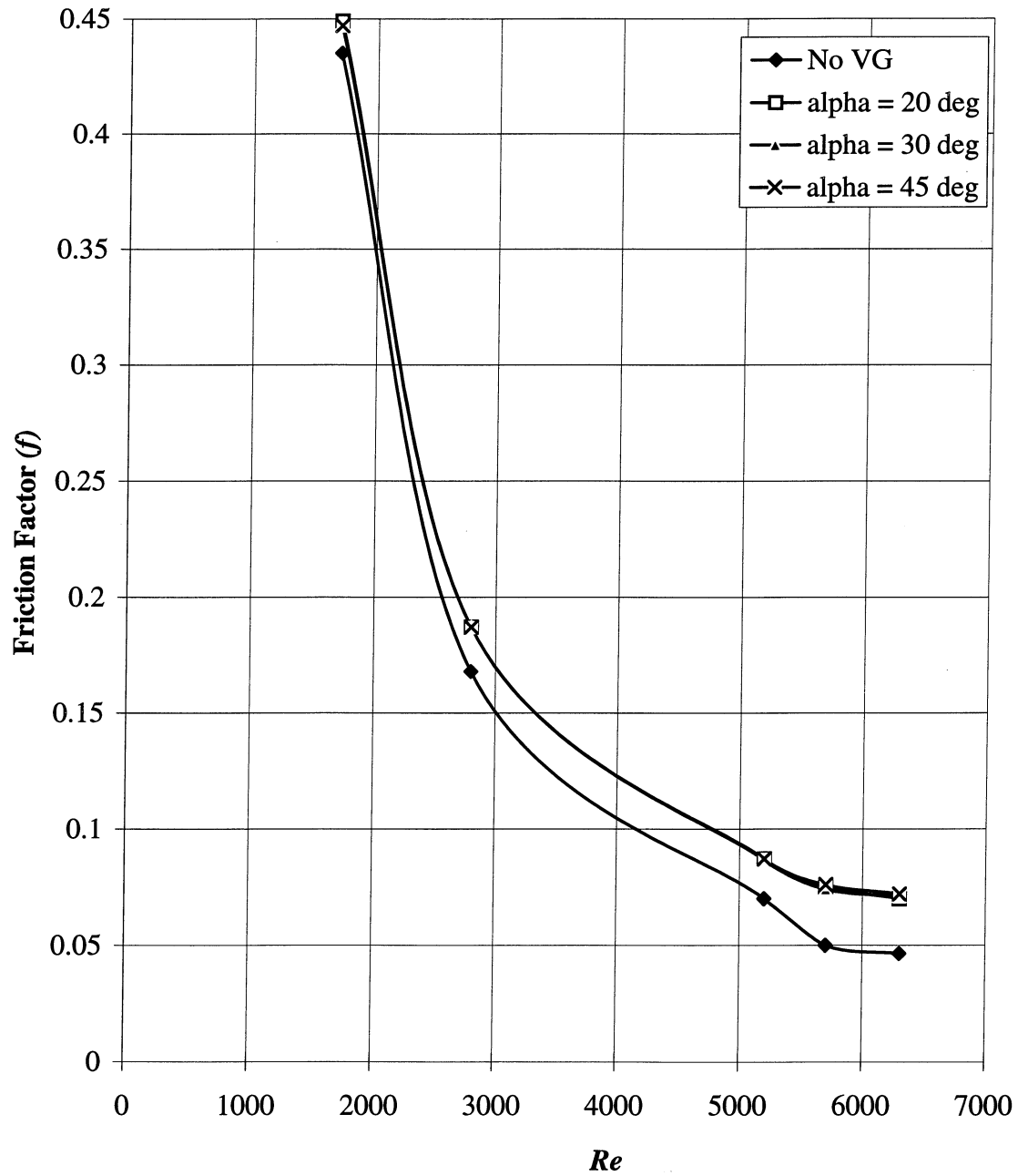


Figure 3.15 - Fanning friction factor versus Re for a delta-wing VG with an $\Lambda = 4.0$.

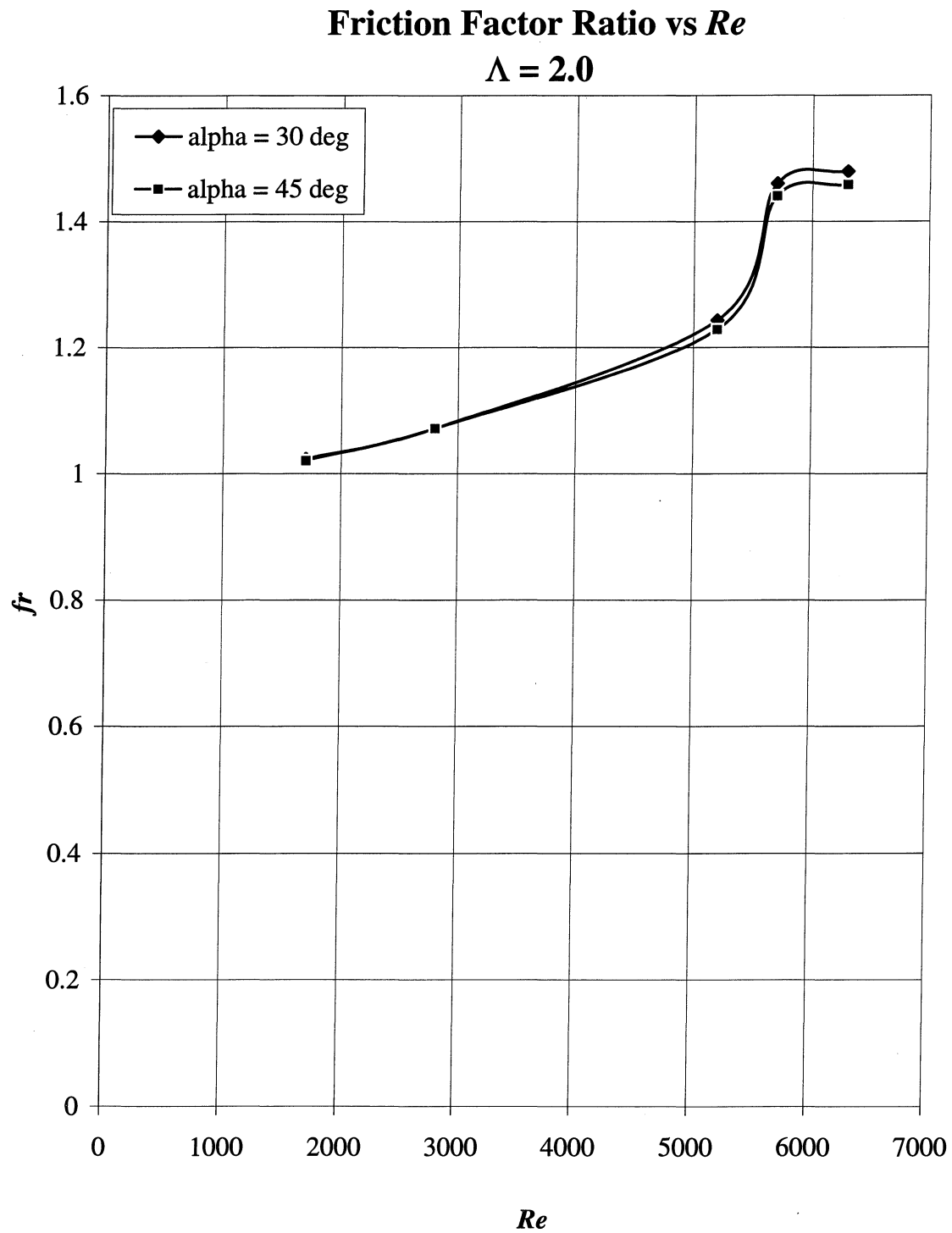


Figure 3.16 - Friction factor ratio (fr) versus Re for a delta-wing VG with an $\Lambda = 2.0$.

Friction Factor Ratio vs Re

$$\Lambda = 4.0$$

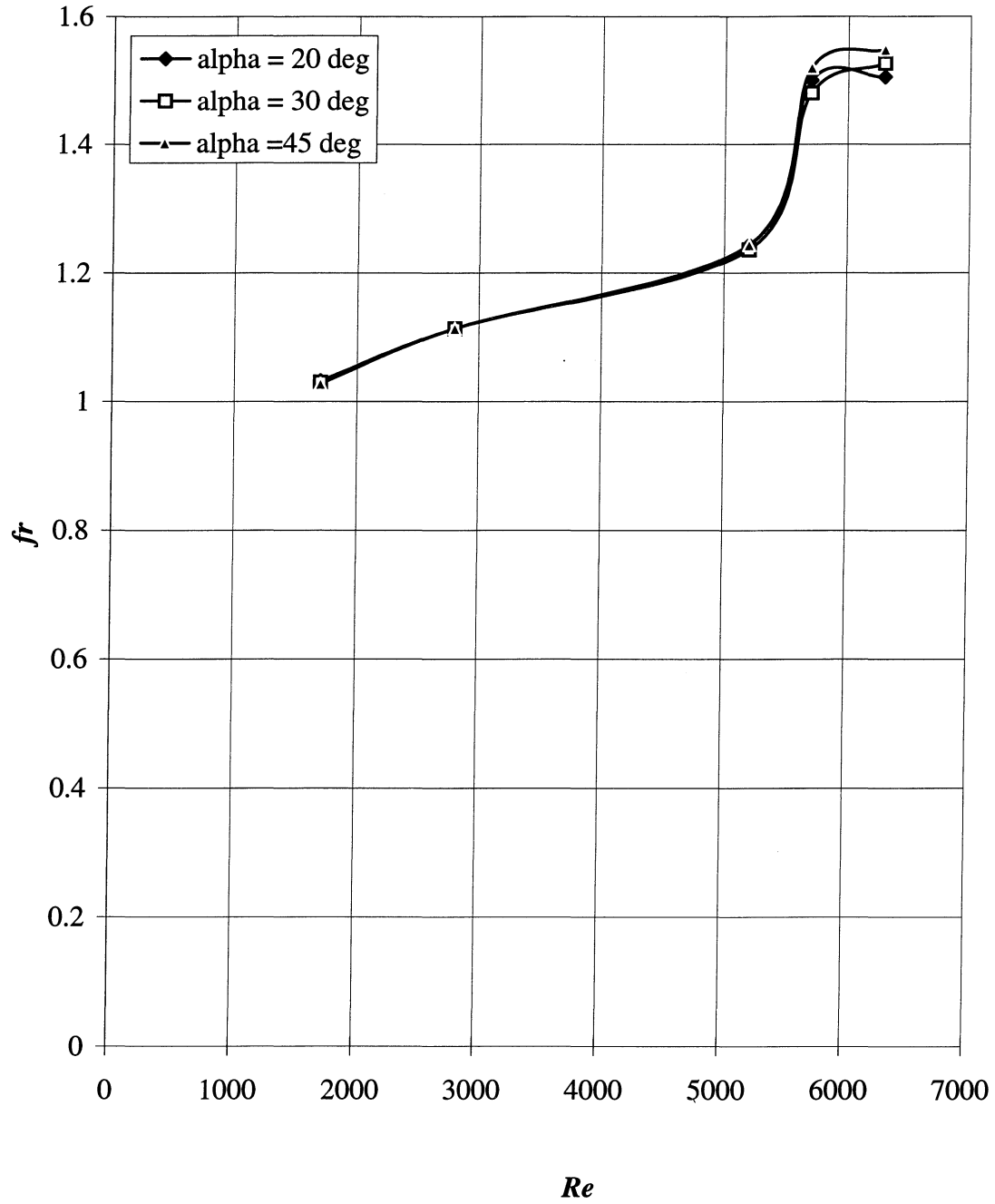


Figure 3.17 - Friction factor ratio (fr) versus Re for a delta-wing VG with an $\Lambda = 4.0$.

Chapter 4 - Conclusions and Future Work

4.1 Conclusions

Experiments to determine the local and average heat transfer enhancement, local temperature profiles, and pressure drop penalty for a delta-wing vortex generator mounted at the leading edge of a channel have been performed in this research project. The results indicate substantial average enhancements and modest pressure drop penalties for developing channel flows with Reynolds numbers from 1700 to 6300. The data are summarized in table 4.1, where the potential of this augmentation method is clearly demonstrated. The heat transfer surface area used in this study was 37 to 63 times the vortex generator area. These data support prior research indicating that delta wings can be employed to enhance heat transfer in channel flow conditions. Although a larger heat transfer area was used for the higher aspect ratio delta ($\Lambda = 4.0$), it still produced heat transfer enhancement values comparable to the $\Lambda = 2.0$ delta wing. The experimental techniques used in this study, addressed some drawbacks inherent in prior research based on a hue-temperature correlation for color and temperature. Other conclusions from this study are presented below in the following order: (1) advantages of the liquid crystal thermography (LCT) used in this study, (2) heat transfer enhancements for $\Lambda = 2.0$ and 4.0 vortex generators, (3) pressure drop penalty produced by $\Lambda = 2.0$ and 4.0 vortex generators, and (4) future work for delta-wing vortex generators and LCT research.

- Using a 35mm camera, 24-bit scanner, image processing software, and RGB color space is an effective LCT technique to quantify the color properties of a flat surface coated with TLCs.
- The hue-temperature approach for correlating color and temperature has good resolution in the mid-range of the TLC, but poor resolution occurs in the lower and upper active range. This study addressed these shortcomings by using the RGB color space and developing of a color-temperature lookup table. This modification allowed full use of the TLC temperature bandwidth.

- For the $\Lambda = 2.0$ delta-wing vortex generator, the average heat transfer enhancement increased with angle of attack for a given Re . The peak average heat transfer enhancement (87%) occurred at $Re = 6300$ and $\alpha = 30^\circ$.
- Local heat transfer enhancement values (for the $\Lambda = 2.0$ delta wing) of over 100% were measured in the region where the greatest boundary layer thinning occurred.
- For the $\Lambda = 4.0$ delta-wing vortex generator, the peak average heat transfer enhancement was 103%. As with the $\Lambda = 2.0$ delta wing, this peak occurred at $\alpha = 30^\circ$.
- Local heat transfer enhancement values of over 200% were recorded for the $\Lambda = 4.0$ delta-wing vortex generator.
- When the pressure drop penalty and heat transfer enhancement were considered for the $\Lambda = 2.0$ delta-wing vortex generator, the flow conditions of $Re = 2800$ and $\alpha = 30^\circ$ had the best performance. The comparison was based on the ratio of Nur to fr , and the resulting ratio was 1.4.
- When the pressure drop penalty and heat transfer enhancement for the $\Lambda = 4.0$ delta-wing vortex generator were considered, the best performing condition was $Re = 5200$ and $\alpha = 30^\circ$, where $Nur/fr = 1.7$.
- For the same VG surface area, the higher aspect-ratio delta-wing produced a slightly higher mean heat transfer enhancement than the lower aspect-ratio delta wing; the pressure drop penalty was comparable for both vortex-generator geometries.

Table 4.1 - Impact of Wing-Type Vortex Generators on the Performance of a Simplified Continuous-Fin Heat Exchanger.

Flow Rate		Wing Geometry		Performance Impact		
Face Velocity m/s (ft/s)	Re	Aspect Ratio Λ	Attack Angle α	$\frac{Nu_{enh}}{Nu_o}$	$\frac{f_{enh}}{f_o}$	$\frac{Nu_{enh}f_o}{Nu_of_{enh}}$
.7 (2.3)	1700	2	20	.8	n/a	n/a
			30	1.3	1.0	1.3
			45	.9	1.0	.9
		4	20	1.5	1.0	1.5
			30	1.2	1.0	1.2
			45	1.2	1.0	1.2
1.2 (3.9)	2800	2	20	1.0	n/a	n/a
			30	1.5	1.1	1.4
			45	1.4	1.1	1.3
		4	20	1.3	1.1	1.2
			30	1.3	1.1	1.2
			45	1.3	1.1	1.2
2.0 (6.6)	5200	2	20	1.1	n/a	n/a
			30	1.5	1.2	1.3
			45	1.5	1.2	1.3
		4	20	1.2	1.2	1.0
			30	2.0	1.2	1.7
			45	1.5	1.2	1.3
2.6 (8.5)	6300	2	20	1.2	n/a	n/a
			30	1.9	1.5	1.3
			45	1.6	1.5	1.1
		4	20	1.7	1.5	1.1
			30	1.9	1.5	1.3
			45	1.8	1.6	1.1

n/a - Data is not available.

4.2 Future Work

In this study, new thermochromic liquid crystal data have been provided to quantify the heat transfer enhancement performance of delta-wing vortex generators in a channel flow configuration. Basing the heat transfer on the area impacted by the vortex generator demonstrates the potential of using multiple generators to enhance heat transfer. The liquid crystal thermography technique showed that the deficiencies of the hue-temperature relation (poor resolution in the upper and lower band of the TLC) could be overcome by using a RGB color space and color-temperature lookup table.

Although this study provided a method for effectively relating color and temperature and a deeper understanding of heat transfer enhancement produced by delta-wing vortex generators, there are several related areas where further work is needed. Recommendations for future work are made in the following areas: LCT technology, the effects of streamwise vortices in channel flows, and the impact of heat transfer enhancement on heat exchanger volume reduction.

- LCT Method
 - The impact of the lighting angle on the repeatability of the color-temperature table should be clarified.
 - TLC bandwidth effects on temperature uncertainty should be quantified.
 - It would be interesting to explore alternative color representations (e.g., CMYK).
- Streamwise Vortices in Channel Flow
 - The impact of aspect ratio and angle of attack on circulation should be studied, and circulation should be quantitatively related to heat transfer.

- Vortex decay in channel flows should be studied further to provide guidance in their application to heat exchangers.
 - Alternative locations for the vortex generator - other than the leading edge - should be considered.
- Heat Exchangers
 - Quantify the potential heat exchanger volume reduction as a result of using delta-wing vortex generators.
 - Study full-scale heat exchangers with delta-wing and winglet vortex generators to quantify the heat transfer enhancement and pressure drop penalty.
 - Study the impact that vortex generators would have on frost and condensation formation.

A - Experimental Methods for Liquid Crystal Thermography

This appendix describes the liquid crystal thermography (LCT) method used in this study. LCT is a means of relating color behavior and temperature of a surface coated with thermochromic liquid crystals (TLCs). This LCT method was accomplished in three steps:

1. Assembly of the test model (prototype plate heat exchanger)
2. TLC preparation and application technique
3. Calibration and digitization of thermochromic liquid crystal (TLC) images

The equipment used for this liquid crystal thermography procedure consisted of a wind tunnel, 35mm camera, lighting, computer, and CCD scanner (figures 2.1 and 2.5). A 35mm camera with telephoto lens and light source were positioned in front of the test section. This arrangement allowed the recording of the TLC images for the entire color-play range and was used for both calibration and heat transfer experiments.

Assembly of Test Model - The prototype plate heat exchanger (figure 2.2) consisted of five parallel plates (representing fins), and the center plate was the test specimen. A foil heater was fixed to the center plate, and a thermocouple was attached to each corner of a 1.9 cm x 1.35 cm area on the unexposed side of the foil heater. The thermocouples were adhered to the heater surface with Thermoset (340 resin) epoxy. In the area where thermocouples were attached, foam insulation (.31 cm thick) was applied to the unheated side of the center plate. The temperature readings of the four thermocouples were averaged to determine the surface temperature of the 1.9 cm x 1.35 cm area (figure A.1). These average surface temperature values were used in the development of the color-temperature lookup table (table B.1).

Prior to adhering the thermocouples to the heater surface, they were calibrated simultaneously; the calibration was performed using a NesLab isothermal bath and mercury-in-glass thermometers with .01 °C divisions. Since these thermometers were

total immersion thermometers, the temperature readings were corrected to account for the section of the thermometer that was exposed to the air (see DeJong[45] for more discussion about the thermometer correction procedure). The thermocouples were calibrated in 2° C increments over a 24 to 38° C range.

Before mounting the test model in the wind tunnel, the center plate was sprayed with TLC and prepared for recording the heat transfer surface images.

TLC Surface Preparation and Application Technique - The thermochromic liquid crystal (TLC) surface preparation for the middle test plate consisted of three steps: diluting, mixing and spraying. After the foil heater was adhered to the middle test fin, several light coats of water-based black paint were applied by an air brush. The paint aided in obtaining a vibrant display of the visible spectrum of the TLC paint. Following the black paint, the diluted well-mixed TLC (~1 μm thick) was applied with an air brush.

Diluting the TLC mixture improved the spray and adhesion to heat transfer surface. The diluted mixture was 1/6 tap water, 1/6 alcohol, and 2/3 TLC encapsulated paint by volume (at room temperature). The solution was mixed well by shaking the three fluids until no particles resided in the bottom of the mixture holder. An air brush was used to apply the TLC with a brisk random motion of the air brush pointer. A high air to TLC ratio allowed the TLC to be applied in extremely thin coats and this application technique was critical for obtaining the desired color brilliance for the images.

In preparation of the color-temperature calibration, the TLC-coated surface was illuminated with a white light source. When a TLC-coated surface is illuminated with a light source at fixed angle, it reflects only one color at a unique temperature; this temperature must be in the range of the liquid crystal. As the temperature of the TLC coated surface was increased, the reflected color went from red in the lower temperature range to blue at higher temperature values. At temperature values below and above the bandwidth, the TLC-coated surface appeared black.

Calibration and Digitalization of TLC Images - The next step in the LCT process was calibrating and digitizing images of the TLC coated surface. First, a set of standard or reference colors were developed, and they were used to establish a color look-up table. The color lookup table is a method for storing color behavior data[48]; see appendix B for more discussion on color behavior and development of a color lookup tables. In addition to the color behavior data, this color lookup table stored the temperature associated with the reference color. Henceforth, a color table that also includes temperature data will be referred to as a color-temperature lookup table. In order to determine the color behavior data, the TLC images were transformed into a digital image format.

For repeatability of the color during the heat transfer experiments, the camera and light source were positioned in the same location as the calibration phase. Research by Moffat[28] has demonstrated that altering the viewing angle and light source can impact the perceived color and ultimately the predicted temperature value of a TLC coated surface.

Thermocouple Temperature Reading vs Temperature Reading Number

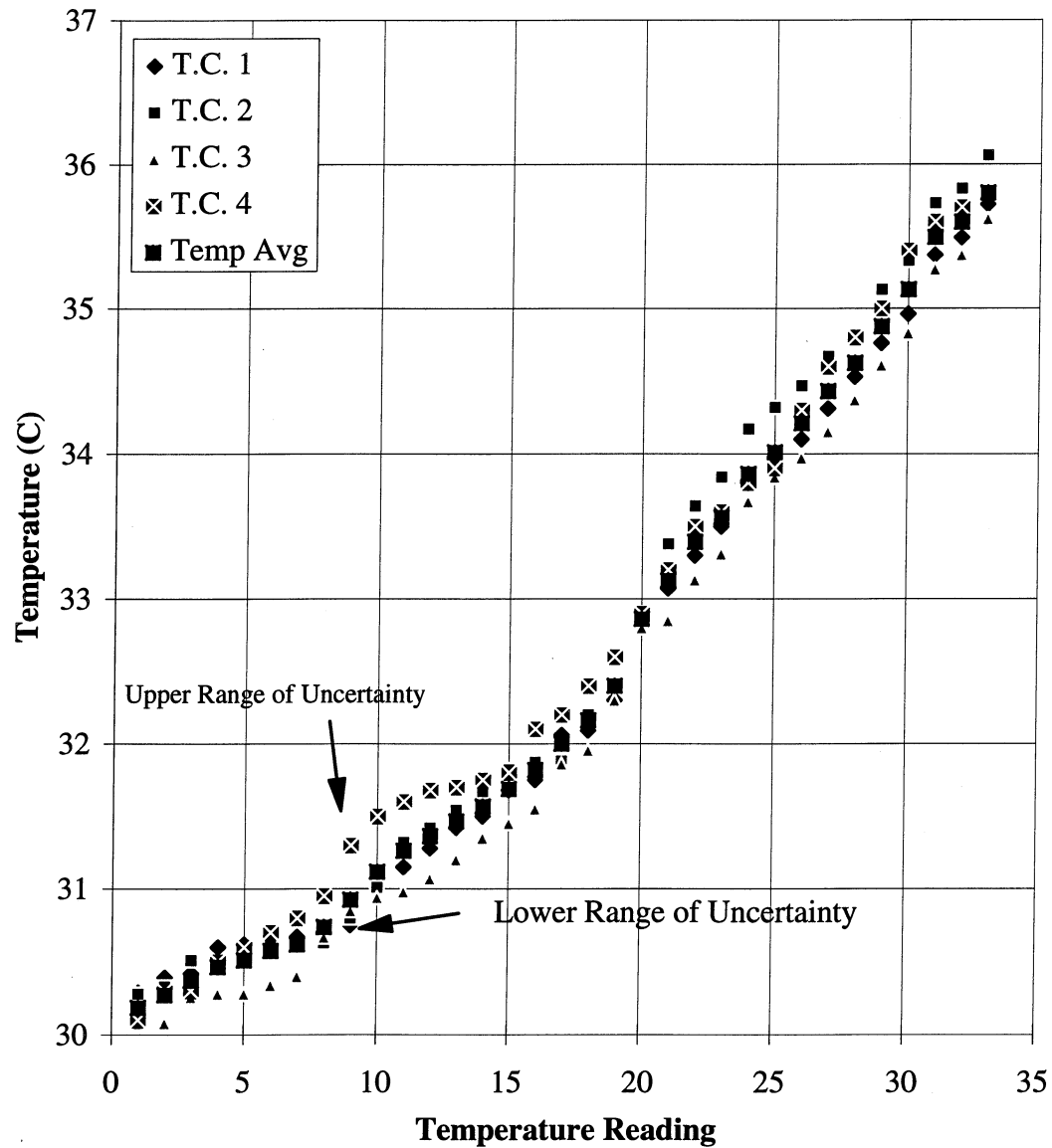


Figure A.1 - Plot of thermocouple readings for color-temperature calibration.

B - Procedure for Developing a Color-Temperature Lookup Table

This appendix discusses the procedure used for developing a color table and the method for relating color and temperature of a surface coated with TLC. First, a method for quantifying color behavior--color model--will be discussed. This will be followed by a discussion on how quantification of color behavior can be used to develop a color table. Lastly, the application of the color table for predicting temperature will be reviewed.

Color Model - A color model is a method for explaining and quantifying the properties or behavior of color within a particular context, and it usually relies on the dominant wavelength for identifying the color or hue. Typically, color models that are used to describe combinations of light in terms of the dominant wavelength (hue or color) use three primary colors to obtain a wide range of colors, known as the color table or color gamut [39]. For this study, the red, green, blue (RGB) color model was used to quantify the color properties of digitized images. The weighting of colors is a standard that was created in 1931 by the International Commission on Illumination (Commission Internationale de l'Eclairage[39], also called the CIE). The purpose of the standard was to develop a means of defining other colors in a color model based on the weighted sum of the three primary color

According to Foley[39], our eyes perceive color through the stimulation of three visual pigments in the cones of the retina. These three pigments have a peak intensity of about 630 nm, 530 nm, and 450 nm for red, green, and blue, respectively. This tri-stimulus theory of vision is the basis for displaying the color output on a video monitor with the three primary colors (red, green, and blue) referred to as the RGB color model [48]. For this study, the RGB color model was highly convenient and appropriate for the image processing system used to relate color and temperature, since the scanned images were digitized into the RGB color coordinate system. The color model was represented with a cube defined on the R, G, B axes as shown in figure B.1[48]. The origin represented black, and the vertices with coordinates (1,1,1) represented white; For figure B.1, the

RGB vales were normalized. However, the RGB values for this study were not normalized, and the RGB values for each pixel could range from 1 to 255. The vertices of the cube on the axes of figure B.1 represented the primary colors, and the remaining vertices represented the complimentary color for each primary color

Color Table - A color-temperature lookup table is a means of storing color and temperature data for future use. This color-temperature lookup table was developed by scanning 33 TLC images with a 24-bit CCD color scanner at a resolution of 800 dots per inch. Each pixel of the referenced images was assigned a RGB value and the median RGB values were used for development of the lookup table (see table B.1). For example, the TLC coated surface with a temperature of 30.2° C produced RGB median values of 84, 58, and 37, respectively. Table B.1 also has the standard deviation values for the RGB data; however, these data were not used for the data reduction. The RGB data for each image were determined from the scanned data, and then each image was assigned its appropriated RGB values and surface temperature. In addition, the scanned images were given a color table position.

Two hundred fifty-five color table positions were available, and this equated to the number of colors the computer monitor could produce. Since only 33 color-temperature table positions were used, the remaining 222 color table positions did not have any RGB data. The determination of the color table position was represented by the following expression[49]:

$$CTP = 254 \left(\frac{T_s - T_{LB}}{T_{HB} - T_{LB}} \right) + 1 \quad (B1)$$

where CTP represents the color table position, T_s is the average surface temperature of the recorded calibration images, T_{LB} is the lower band temperature of the TLC, and T_{HB} is the higher temperature band of the TLC. Each color table position had its own RGB values.

Predicting the surface temperature is the major advantage of the color-temperature lookup table approach. The local surface temperature was determined by comparing the RGB values of the newly scanned images with the reference values in the lookup table. The minimum Euclidean distance between the referenced color and new color RGB values was the criterion used to assign the color table position and temperature values to the new images; see the distance equation below[49]:

$$d^2 = (r-r_i)^2 + (g-g_i)^2 + (b-b_i)^2 \quad (B2)$$

where d is the distance between the color table RGB vector and newly scanned RGB vector, r_i , g_i , and b_i , are the RGB values of the newly scanned image, and r , g , b are the RGB values of the standard color.

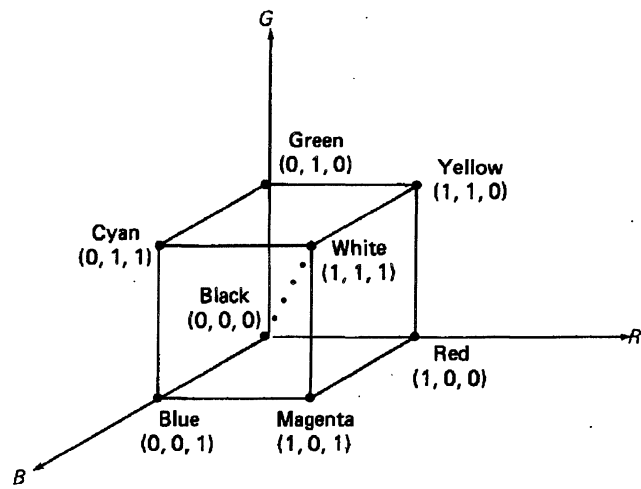


Figure B.1 - Sample RGB color model[48].

Table B.1 - RGB Mean and Standard Deviation Values for TLC Surface

Temperature (°C)	R_{med}	R_{dev}	G_{med}	G_{dev}	B_{med}	B_{dev}
30.2	84	6	58	6	37	3
30.3	97	1.3	68	3	43	.6
30.4	97	3	77	5	44	1
30.5	80	2.8	60	2.5	11	1.2
30.56	83	2.1	65	2.8	15	.8
30.6	93	3.4	51	2.3	12	1.4
30.7	90	2.9	57	3	12	1
30.8	96	2.3	57	2	12	1.4
31.0	81	3.2	66	3.6	8	1
31.2	89	2	116	6	74	7
31.3	95	4	91	3	15	2
31.4	49	0	94	.9	44	1.9
31.5	69	5	110	4	82	6
31.6	78	2.4	83	3	22	2
31.7	49	1	94	1	44	2
31.9	131	3	154	4	62	5
32.0	55	2	92	2	7	1
32.1	49	4	96	2	49	7
32.4	42	2	119	4	11	2
32.9	60	.4	121	2	127	5
33.1	34	1.9	118	3.6	17	1.7
33.4	14	2	107	2	73	4
33.6	29	1.3	86	2.8	20	1.9
33.9	28	1.8	75	3	29	3
34.0	25	1.4	63	3	49	3
34.2	25	1	48	1.4	61	2.8
34.4	10	1.6	74	1.5	89	5
34.6	10	.9	55	1.7	111	3
34.9	23	1	36	1	77	3
35.1	28	.9	35	1	103	5
35.5	28	1	41	1	128	5
35.6	27	.6	31	1	93	4
35.8	33	.8	31	1	99	4

C - Data Reduction Procedure and Uncertainty Analysis

Data Reduction Procedure

Reducing the data and performing the uncertainty analysis required the calculation of the following parameters: (1) Reynolds number, (2) Nusselt number (enhanced and unenhanced), (3) Nusselt number ratio, and (4) friction factor.

The Reynolds number (Re) values were calculated based on the hydraulic diameter and the expression used for the calculation was:

$$Re = \frac{U_c D_h}{\nu_a} \quad (C1)$$

where U_c was the velocity based on the minimum flow cross-sectional area, D_h was the hydraulic diameter, and ν was the kinematic viscosity. Kays and London[50] provided a correlation for the kinematic viscosity of air, and a definition for the hydraulic diameter:

$$\nu_a = \frac{1.8e-5 + 4.8(10e-8) \cdot (T - 290)}{\rho_a} \quad (C2)$$

$$D_h = \frac{4A_c}{A_{ht}} L \quad (C3)$$

where T was the air temperature in Kelvin, ρ_a was the density of the fluid (air), A_c was the flow cross sectional area, A_{ht} was the total heat transfer area. The flow cross sectional area and total heat transfer area were defined accordingly:

$$A_c = A_{ts} - (\delta_p N_p H) \quad (C4)$$

$$A_{ht} = 2 \{ (\delta_p (N_p + 1)H) + (L(N_p + 1)H) \} \quad (C5)$$

where L was the flow length of the prototype heat exchanger, δ_p was the plate fin thickness, H was the plate fin height, and N_p represented the number of plate fins.

The mass flow of the air was determined by measuring the pressure drop across an ASME standard orifice plate, which was calculated using the following formula:

$$m_{op} = KA_{op} \sqrt{2\rho_a \Delta p} \quad (C6)$$

where ΔP was the pressure drop across the orifice plate, β was the diameter ratio, A_{op} was the orifice plate cross-sectional area, and K was the flow coefficient. Expressions for the above parameters were[51]:

$$K = \frac{C}{\sqrt{1 - \beta^4}} \quad (C7)$$

$$C = .5959 + .0321\beta^{2.1} - .184\beta^8 + .039 \frac{\beta^4}{(1 - \beta^4)} - .01685\beta^3 + 91.71\beta^{2.5} \text{Re}_{D_h}^{-.75} \quad (C8)$$

$$\beta = D_{op}/D_p \quad (C9)$$

where D_{op} was the orifice plate diameter, D_p was the pipe diameter, β was the diameter ratio, and C was the discharge coefficient.

After the mass flow rate was determined, the velocity based on flow cross-sectional was determined:

$$U_c = \frac{m_{op}}{\rho_a A_c} \quad (C10)$$

$$U_c = K \frac{A_{op}}{\rho_a A_c} \sqrt{2\rho_a \Delta p} \quad (C11)$$

$$Re = K \frac{A_{op}}{\rho_a A_c} \sqrt{2\rho_a \Delta p} \left(\frac{D_h}{\nu_a} \right) \quad (C12)$$

a. Nusselt Number - Determining the convective heat transfer was critical in measuring the performance-enhancing capability of the vortex generators, and the Nusselt number (Nu) was employed to represent the convective heat transfer. The Nusselt number is equivalent to the dimensionless temperature gradient at the heat exchanger surface, and it provided a means of using a nondimensional parameter for representing the convective heat transfer at the heat exchanger surface. Equation C13 was the expression used to define the local Nusselt number ($Nu(x,y)$) and equation C14 defined the local convective heat transfer ($h(x,y)$):

$$Nu(x,y) = \frac{h(x,y)D_h}{k_f} \quad (C13)$$

$$h(x,y) = \frac{q''_s}{T_s(x,y) - T_m} \quad (C14)$$

where D_h was the hydraulic diameter for the plate heat exchanger and represented the characteristic length, and k_f was the thermal conductivity of the fluid (air) in the test section. For the local convective heat transfer equation (C15), q''_s was the surface heat

flux, $T_s(x,y)$ was the local surface temperature, and T_m was the bulk fluid temperature. Liquid crystal thermography (LCT) was employed to measure the heat transfer surface temperature, and one RTD placed upstream of the heat exchanger was used to measure the approach temperature. See appendices A and B for greater detail on TLC and LCT.

From the foregoing local results, the average Nusselt number was determined, and it was defined as:

$$\overline{Nu} = \frac{\bar{h} D_h}{k_f} \quad (C16)$$

where \bar{h} was the average heat transfer coefficient. The average heat transfer coefficient and heat transfer surface temperature were defined as:

$$\bar{h} = \frac{q''_s}{\overline{T_s} - T_m} \quad (C17)$$

$$\overline{T_s} = \frac{1}{A_s} \int T(x, y) dA_s \quad (C18)$$

Image software package was used to perform the integration and ultimately determine the plate fin surface temperature.

b. Nusselt Number Ratio - Determining the heat transfer enhancement produced by the vortex generators required relating the enhanced and unenhanced Nusselt number, and this relation was designated as the Nusselt number ratio (Nur). The local and average Nusselt number ratio values were defined as:

$$Nur(x, y) = \frac{Nu_{enh}(x, y)}{Nu_o(x)} \quad (C19)$$

$$\overline{Nur} = \overline{Nu_{enh}} / \overline{Nu_o} \quad (C20)$$

where Nu_{enh} and Nu_o were the enhanced and unenhanced Nusselt numbers, respectively. The average and local values of the Nusselt number were determined based on the average and local temperature values, respectively. Lastly, Nur was calculated for various conditions such as delta wing angle attack and aspect ratio to determine the impact of these parameters on heat transfer enhancement.

c. Friction Factor - Pressure drop data were represented using the Fanning friction factor, which was defined as:

$$f = \frac{\Delta p D_h}{2 \rho_a U^2 L} \quad (C21)$$

where ΔP was the pressure drop across the prototype heat exchanger and L was the heat exchanger length. The friction factors, for conditions with and without the vortex generators, were used to determine the pressure drop penalty produced by the vortex generators. This ratio was known as the friction factor ratio, which was defined as:

$$fr = f_{enh} / f_o \quad (C22)$$

where fr represented the friction factor ratio, f_{enh} was the friction factor with vortex generators, and f_o was the friction factor without vortex generators.

Uncertainty Analysis

Applying the uncertainty analysis discussed by Fox and McDonald[52], the uncertainty in the Reynolds number was expressed as:

$$\frac{W_{Re}}{Re} = \left[\left(\frac{W_{U_c}}{U_c} \right)^2 + \left(\frac{W_{D_h}}{D_h} \right)^2 + \left(\frac{W_v}{v_a} \right)^2 \right]^{1/2} \quad (C23)$$

where W_{Re} = the uncertainty in the Reynolds number

W_{D_h} = the uncertainty in hydraulic diameter

W_v = the uncertainty in kinematic in the viscosity.

For the flow cross-sectional area velocity (U_c), the uncertainty was determined by propagating errors through the continuity equation, as shown in C24:

$$\frac{W_{U_c}}{U_c} = \left[\left(\frac{W_{\dot{m}}}{\dot{m}} \right)^2 + \left(\frac{W_{\rho_a}}{\rho_a} \right)^2 + \left(\frac{W_{A_c}}{A_c} \right)^2 \right]^{1/2} \quad (C24)$$

The uncertainty in the mass flow rate was determined by using the following formula:

$$W_{\dot{m}} = \left[\left(W_D \frac{\partial \dot{m}}{\partial D} \right)^2 + \left(W_c \frac{\partial \dot{m}}{\partial C} \right)^2 + \left(W_\rho \frac{\partial \dot{m}}{\partial \rho_a} \right)^2 + \left(W_\beta \frac{\partial \dot{m}}{\partial \beta} \right)^2 + \left(W_{\Delta P} \frac{\partial \dot{m}}{\partial \Delta P} \right)^2 \right]^{1/2} \quad (C25)$$

For the velocity range of this study, the above equation (C25) was used to predict an uncertainty value of $\pm 1.94\%$ for the Re . The uncertainty was based the following uncertainty values. The uncertainty for the discharge coefficient, based on the ASME standard[52], was a function of Re and orifice plate geometry. For this study, the uncertainty was $.2\%$. The uncertainty in the diameter ratio was 1.4% and in the pipe diameter was $.7\%$. The uncertainty in the ΔP was determined based on the velocity range of the experiments in this study; the uncertainty was $.6\%$. The air density was corrected for the temperature changes and the error was $.5\%$ [53].

Similarly for the Nusselt number, the application of the uncertainty prediction technique discussed by Fox and McDonald[52] yielded the following expression:

$$\frac{W_{Nu}}{Nu} = \left[\left(\frac{W_{\Delta T}}{\Delta T} \right)^2 + \left(\frac{W_{q_s}}{q_s} \right)^2 + \left(\frac{W_{k_f}}{k_f} \right)^2 \right]^{1/2} \quad (C26)$$

where W_{Nu} = the uncertainty in the Nusselt number

$W_{\Delta T}$ = the uncertainty in the temperature difference between the heat surface and bulk fluid temperature values

W_{q_s} = the uncertainty in the heat flux of the plate fin heater

W_k = the uncertainty in the thermal conductivity of the fluid.

For the experiments reported in this study, equation C26 was used to predict a typical uncertainty value of $\pm 5.47\%$ for Nusselt number. The uncertainty was based on a temperature uncertainty of $\pm .3^\circ \text{C}$, a heat flux uncertainty of $\pm .5\%$, and thermal conductivity of uncertainty of $\pm .5\%$ [53].

The formula for determining friction-factor uncertainty was:

$$\frac{W}{f} = \left[\left(\frac{W_{\rho_a}}{2\rho_a} \right)^2 + \left(\frac{W_{\Delta P}}{\Delta P} \right)^2 + \left(\frac{W_{U_c}}{U_c} \right)^2 \right]^{\frac{1}{2}} \quad (C28)$$

where W_f = the uncertainty of the friction factor

W_{ρ} = the uncertainty of the density

W_U = the uncertainty of the velocity

$W_{\Delta P}$ = the uncertainty of the pressure drop across the core.

For the velocity range of this experiment, the air density, flow cross-sectional area velocity and pressure drop were .6%, 1.94% and 10% respectively. The resulting friction factor uncertainty was 10.2%.

D Non-Dimensional Data

Because of the complexity of the fluid motion and energy transfer, it is extremely difficult to analytically solve convective heat-transfer problems except for idealized simple cases. Thus, for most engineering problems of practical interest, convective heat transfer is studied experimentally in the form of empirical expressions that involve dimensionless groups. The advantage of using dimensionless groups for a correlation is that several variables are combined into a few; hence the quantity of variables studied are reduced to a manageable level. The dimensionless groups may be determined from the dimensionless form of the equations governing the physical process. The dimensional equations are applied first; then the dimensionless form of the differential equations governing the physical process are employed to determine the appropriate dimensionless group.

The assumptions used in the analysis are:

- constant property flow
- three-dimensional, incompressible, steady, Newtonian flow
- no body forces, neglect viscous dissipation

The dimensional equations of motion and energy are as follows:

Continuity:
$$\frac{\partial u}{\partial x} + \frac{\partial v}{\partial y} + \frac{\partial w}{\partial z} = 0 \quad (D1)$$

x-Momentum:
$$\rho \left(u \frac{\partial u}{\partial x} + v \frac{\partial u}{\partial y} + w \frac{\partial u}{\partial z} \right) = -\frac{\partial p}{\partial x} + \mu \left(\frac{\partial^2 u}{\partial x^2} + \frac{\partial^2 u}{\partial y^2} + \frac{\partial^2 u}{\partial z^2} \right) \quad (D2)$$

y-Momentum:
$$\rho \left(u \frac{\partial v}{\partial x} + v \frac{\partial v}{\partial y} + w \frac{\partial v}{\partial z} \right) = -\frac{\partial p}{\partial y} + \mu \left(\frac{\partial^2 v}{\partial x^2} + \frac{\partial^2 v}{\partial y^2} + \frac{\partial^2 v}{\partial z^2} \right) \quad (D3)$$

z-Momentum:
$$\rho \left(u \frac{\partial w}{\partial x} + v \frac{\partial w}{\partial y} + w \frac{\partial w}{\partial z} \right) = - \frac{\partial p}{\partial z} + \mu \left(\frac{\partial^2 w}{\partial x^2} + \frac{\partial^2 w}{\partial y^2} + \frac{\partial^2 w}{\partial z^2} \right) \quad (\text{D4})$$

Energy:
$$\rho c_p \left(u \frac{\partial T}{\partial x} + v \frac{\partial T}{\partial y} + w \frac{\partial T}{\partial z} \right) = k \left(\frac{\partial^2 T}{\partial x^2} + \frac{\partial^2 T}{\partial y^2} \right) \quad (\text{D5})$$

The nondimensional form of the above equations is obtained by using the characteristic length L , a reference velocity of u_∞ , a reference temperature of T_e , a reference temperature difference of $q_s D_h / k_f$, and introducing the following dimensionless variables:

$$X = \frac{x}{L} \quad Y = \frac{y}{L} \quad P \equiv \frac{p}{\rho u_\infty^2} \quad (\text{D6})$$

$$U = \frac{u}{u_\infty} \quad V = \frac{v}{v_\infty} \quad \Theta = \frac{T - T_e}{q_s D_h / k_f} \quad (\text{D7})$$

The quantity ρu_∞^2 used to nondimensionalize the pressure represents twice the dynamic pressure. By introducing the above variables (Eqs. D6 and D7), one is able to obtain the continuity, momentum, and energy equations in the dimensionless form:

Continuity:
$$\frac{\partial U}{\partial X} + \frac{\partial V}{\partial Y} + \frac{\partial W}{\partial Z} = 0 \quad (\text{D8})$$

$$\text{X-momentum:} \quad U \frac{\partial U}{\partial X} + V \frac{\partial U}{\partial Y} + W \frac{\partial U}{\partial Z} = -\frac{\partial P}{\partial X} + \frac{1}{\text{Re}} \left(\frac{\partial^2 U}{\partial X^2} + \frac{\partial^2 U}{\partial Y^2} + \frac{\partial^2 U}{\partial Z^2} \right) \quad (\text{D9})$$

$$\text{Y-momentum:} \quad U \frac{\partial V}{\partial X} + V \frac{\partial V}{\partial Y} + W \frac{\partial V}{\partial Z} = -\frac{\partial P}{\partial Y} + \frac{1}{\text{Re}} \left(\frac{\partial^2 V}{\partial X^2} + \frac{\partial^2 V}{\partial Y^2} + \frac{\partial^2 V}{\partial Z^2} \right) \quad (\text{D10})$$

$$\text{Z-momentum:} \quad U \frac{\partial W}{\partial X} + V \frac{\partial W}{\partial Y} + W \frac{\partial W}{\partial Z} = -\frac{\partial P}{\partial Z} + \frac{1}{\text{Re}} \left(\frac{\partial^2 W}{\partial X^2} + \frac{\partial^2 W}{\partial Y^2} + \frac{\partial^2 W}{\partial Z^2} \right) \quad (\text{D11})$$

$$\text{Energy:} \quad \left(U \frac{\partial \Theta}{\partial X} + V \frac{\partial \Theta}{\partial Y} + W \frac{\partial \Theta}{\partial Z} \right) = \frac{1}{\text{Re Pr}} \left(\frac{\partial^2 \Theta}{\partial X^2} + \frac{\partial^2 \Theta}{\partial Y^2} + \frac{\partial^2 \Theta}{\partial Z^2} \right) \quad (\text{D12})$$

where the dimensionless groups are defined as:

$$\text{Pr} \equiv \frac{\nu}{\alpha} = \text{Prandtl number} \quad (\text{D13})$$

$$\text{Re} \equiv \frac{u_{\infty} L}{\nu} = \text{Reynolds number.} \quad (\text{D14})$$

The heat transfer coefficient is one the parameters one wants to compute in a heat transfer analysis. The heat transfer coefficient is defined as:

$$h \equiv \frac{q_s''}{\Delta T} \quad (\text{D15})$$

where q_s'' is defined as the heat flux and ΔT is the difference between the surface and mean fluid temperatures. The mean fluid temperature is known as the bulk fluid

temperature, which is defined by the following expression:

$$T_m = \frac{1}{A_c U_c} \int_{A_c} u T dA_c \quad (\text{D18})$$

where U_c is the mean free-flow velocity and A_c is the flow cross-sectional area.

E - Vortex Generator Geometry Selection

This appendix discusses the selection of the vortex geometries used in this study.

Two delta-wing geometries, aspect ratio values of 2 and 4, were used in this study. A summary of the velocity and angle of attack conditions are summarized in table E.1.

Table E.1 - Summary of Delta-Wing Geometry and Experimental Conditions

<i>Aspect Ratio (Λ)</i>	<i>Reynolds Number (Re)</i>	<i>Alpha (α)</i>
2.0	1700, 2800, 5200, 6300	20, 30, 45 Deg
4.0	1700, 2800, 5200, 6300	20, 30, 45 Deg

Selection of the vortex generator geometry and aspect ratio was based on published reports [4, 9, 23, 54-56] that indicated delta wings would provide high heat transfer enhancement for the Re range considered. Bragg[57] reported, based on experimental investigations of high lift wings, that delta wings were good vortex generators for delaying boundary layer separation; the separation was delayed by thinning the momentum boundary layer. Since the momentum and thermal boundary layers for air are the same order of magnitude ($Pr \sim 1$), a method that thins the momentum boundary layer would also be effective in thinning the thermal boundary layer. Thus, one would infer that delta-wing vortex generators are effective momentum and thermal boundary layer thinners for air as the working fluid.

As discussed in chapter 1, published literature also indicated that high aspect ratio wings and high angle of attack wings were good design features for high circulation; thus good design features for high lift. Keuthe and Chow[10] explained that delta-wing lift increased with circulation for a given velocity. As can be seen from figures 3.2 and 3.3, the slope of the lift curve is higher for delta wings with larger aspect ratios. In addition, Barber et al.[58] reported that vortex circulation of delta-wing vortex generators increased with aspect ratio. In chapter 1, it was noted that the downwash velocity was proportional to

circulation. Heat transfer reports[17, 20, 22] have indicated thermal boundary thinning is related to the downwash velocity created by the vortex generators. Although the higher aspect ratio delta-wing vortex generators generate larger induced vorticity, Barber[58] observed that the stronger vortices created by the higher aspect ratio delta wings convected more quickly away from the wall surface than weaker vortices created by low aspect ratio wings. Percy[59] also noted that vortex generators with a small wing base tend to persist longer due to the interaction of the counter-rotating vortices. Similar results can be expected for developing channel flow configurations.

LIST OF REFERENCES

1. Incropera, F.P., and DeWitt, D. P., *Fundamentals of Heat Transfer and Mass Transfer*, 3rd edition, John Wiley , New York. 1990.
2. Webb, R. L., *Principles of Enhanced Heat Transfer*, John Wiley, New York, 1994.
3. Sukhatme, S. P., and Devotta, S., "Classification of Heat Transfer Equipment," in *Heat Transfer Design*, eds., R. K. Shah, E. C. Subbarao, and R. A. Mashekar , Hemisphere Publishing Co., New York, 1988.
4. Jacobi, A. M., and Shah, R. K., "Heat Transfer Surface Enhancement Through the Use of Longitudinal Vortices: A Review of Recent Progress," *Experimental Thermal and Fluid Science*, **11**:295-309, 1995.
5. Gentry, M. C., "Heat Transfer Enhancement on a Flat Plate Using Delta-Wing Vortex Generators," M.S. Thesis, Department of Mechanical and Industrial Engineering, University of Illinois, Urbana, IL 1995.
6. Batchelor, G. K., *An Introduction to Fluid Dynamics*, Cambridge University Press, Cambridge, 1992.
7. Fiebig, M., Kallweit, P., and Mitra, N., "Wing Type Vortex Generators for Heat Transfer Enhancement," *Heat Transfer 1986, Proceedings of the Eighth International Heat Transfer Conference*, **6**:2909-2913, Hemisphere Publishing, New York, 1986.
8. Russell, C. M., Jones, T. V., and Lee G. H., "Heat Transfer Enhancement Using Vortex Generators," *Heat Transfer 1982, Proceedings of the Seventh International Heat Transfer Conference*, **3**:283-288, Hemisphere Publishing, New York, 1982.
9. Tiggelbeck, S. T., Mitra, N. K., and Fiebig, M., "Comparison of Wing-Type Vortex Generators for Heat Transfer Enhancement in Channel Flows," *Journal of Heat Transfer*, **116**:880-885, 1994.
10. Kuethe, A. M, and Chow C-Y, *Foundations of Aerodynamics: Bases of Aerodynamic Design*, 4th edition, John-Wiley & Sons, New York, 1986.

11. Lachmann, G. V., *Boundary Layer and Flow Control: Its Principles and Application*, Pergamon Press Inc., 1961.
12. McCormick, B. W., *Aerodynamics, Aeronautics, and Flight Mechanics*, John Wiley, 1995.
13. Wedermeyer, E., "Vortex Breakdown," *High Angle of Attack Aerodynamics*, AGARD Lecture Series No. 121, December 1982.
14. Jones, R. T., *Wing Theory*, Princeton University Press, 1990.
15. Wentz, W. H., and Kohlman, D. L., "Vortex Breakdown on Slender Sharp-Edged Wings," *AIAA*, **69-778**, 1969.
16. Johnson, T. R., and Joubert, P. N., "The Influence of Vortex Generators on Drag and Heat Transfer From a Circular Cylinder Normal to an Airstream," *Journal of Heat Transfer*, **91**:91-99, 1969.
17. Kataoka, K., Doi, H., and Komai, T., "Heat/Mass Transfer In Taylor Vortex Flow with Constant Axial Flow Rates," *International Journal of Heat and Mass Transfer*, **20**:57-63, 1977.
18. Edwards, F. J., and Alker, C. J. R., "The Improvement of Forced Convection Surface Heat Transfer Using Surface Protrusions in the Form of (A) Cubes and (B) Vortex Generators," *Heat Transfer 1974, Proceedings of the Fifth International Heat Transfer Conference*, **2**:244-248, JSME, Tokyo, 1974.
19. Turk, A. Y., and Junkhan, G. H., "Heat Transfer Enhancement Downstream of Vortex Generators on a Flat Plate," *Heat Transfer 1986, Proceedings of the Eighth International Heat Transfer Conference*, **6**:2903-2908, Hemisphere Publishing, New York, 1986.
20. Eibeck, P. A., and Eaton, J. K., "Heat Transfer Effects of a Longitudinal Vortex Embedded in a Turbulent Boundary Layer," *Journal of Heat Transfer*, **109**:16-24, 1987.
21. Zhu, J. X., Mitra, N. K., and Fiebig, M., "Comparison of Numerical and Experimental Results for a Turbulent Flow Field With a Longitudinal Vortex Pair," *Journal of Fluids Engineering*, **115**:270-274, 1993.

22. Fiebig, M., Brockmeier, U., Mitra, N. K., and Guntermann, T., "Structure of Velocity and Temperature Fields in Laminar Channel Flows with Longitudinal Vortex Generators," *Numerical Heat Transfer, Part A*, **15**:281-302, 1989.
23. Fiebig, M., Kallweit, P., Mitra, N., and Tiggelbeck, S., "Heat Transfer Enhancement and Drag by Longitudinal Vortex Generators in Channel Flow," *Experimental Thermal and Fluid Science*, **4**:103-114, 1991.
24. Tiggelbeck, S., Mitra, N., and Fiebig, M., "Flow Structure and Heat Transfer in a Channel with Multiple Longitudinal Vortex Generators," *Experimental Thermal and Fluid Science*, **5**:425-436, 1992.
25. Tiggelbeck, N. K., Mitra, N., and Fiebig, M., "Experimental Investigations of Heat Transfer Enhancement and Flow Losses in a Channel with Double Rows of Longitudinal Vortex Generators," *International Journal of Heat and Mass Transfer*, **36**:2327-2337, 1993.
26. Fiebig, M., "Vortex Generators of Compact Heat Exchangers," *Journal of Enhanced Heat Transfer*, **2**:43-61, 1995.
27. Klein, E., "Liquid Crystals in Aerodynamic Testing," *Astronautics & Aeronautics*, **5**:70-73, July 1968.
28. Moffat, R. J., "Some Experimental Methods for Heat Transfer Studies," *Experimental Thermal and Fluid Science*, **3**:14-32, 1990.
29. Moffat, R. J., "Experimental Heat Transfer," *Proceedings, 9th International Heat Transfer Conference*, Jerusalem, Isarel, **1**:187-205, 1990.
30. Hippensteele, S. A., Russell, L. M., and Stepka, F. S., "Evaluation of a Method for Heat Transfer Measurements and Thermal Visualization Using a Composite of a Heater Element and Liquid Crystals," *Journal of Heat Transfer*, **105**:184-189, 1983.
31. Zharkova, G. M., "Temperature Field Visualization Using Liquid Crystal Method," *Experimental Heat Transfer*, **4**:83-92, 1991.
32. Cooper, T. E., and Groff, J. P., "Thermal Mapping, via Liquid Crystals, of the Temperature Field near a Heated Surgical Probe," *Journal of Heat Transfer*, **73**:250-256, May 1973.

33. Simonich, J. C., and Moffat, R. J., "A New Technique for Mapping Heat Transfer Coefficient Contours," *Review of Science Instrumentation*, **53**:678-683, 1982.
34. Kiomto, H., Iizuka, H., and Hamabe, K., "Precise and Convenient Measurement of the Temperature Profile Appearing on a Temperature-Sensitive Liquid-Crystal Film," *Heat Transfer: Japanese Research, Scripta Technica, Inc*, **0001**:0077-0090., 1992.
35. Ashforth-Frost, S., Edwards, R. J., Graham, D. P., Lovesmith, B. J., Jambunathan, K., and Rhine, J. M., "Measurement of Convective Heat Transfer Coefficients, on Ligaments of a Model Shell Boiler Tube Plate, Using Liquid Crystal Thermography," *ICHEME Symposium Series No. 129*, 352-359.
36. Akino, N., Kunugi, T., Kurosawa, A., Asano, Y., Sagiya, S., and Nakanishi, M., "Thermo-Chromatic Characteristics of Liquid-Crystal Suspensions," *Experimental and Numerical Flow Visualization*, **128**:247-254, 1991.
37. Hollingsworth, D. K., Boehman, A. L., Smith, E. G., and Moffat, R. J., "Application of Liquid of Crystal Thermography to Measurement of Surface Temperature in a Complex Flow," *9th International Heat Transfer Conference*, Jerusalem, Israel, 1990.
38. Pratt, W. K., *Digital Image Processing*, Wiley-Interscience, New York, 1978.
39. Foley, J. D., van Dam, A., Feiner, S. K., and Hughes, J. F., *Computer Graphics: Principles and Practice*, Addison-Wesley Publishing Co., Boston, 1990.
40. Hollingsworth, D. K., Boehman, A., L., Smith, E. G., and Moffat, R. J., "Measurement of Temperature and Heat Transfer Coefficient Distributions in a Complex Flow Using Liquid Crystal Thermography and True-Color Image Processing," *ASME HTD*, **123**:35-42.
41. Farina, D. J., Hacker, J. M., Moffat, R. J., and Eaton, J. K., "Illuminant Invariant Calibration of Thermochromic Liquid Crystals," *Visualization of Heat Transfer Processes, ASME*, **252**:1-11, 1993.
42. Lee, S. J., Lee J. H. and Lee D. H., "Local Heat Transfer Measurements from an lliptic Jet Impinging on a Flat Plate using Liquid Crystal," *International Journal of Heat and Mass Transfer*, **37**:967-976, 1994.

43. Camci, C., Kim, K., Hippensteele, S. A., and Poinsatte, P. E., "Evaluation of a Hue Capturing Based Transient Liquid Crystal Method for High-Resolution Mapping of Convective Heat Transfer on Curved Surfaces," *Journal of Heat Transfer*, **115**:311-318, 1993.
44. Camci, C., Kim, K., and Hippensteele, S. A., "A New Hue Capturing Technique for the Quantitative Interpretation of Liquid Crystal Images Used in Convective Heat Transfer Studies," *Journal of Turbomachinery*, **114**:765-775, 1992.
45. DeJong, N., "An Experimental Study of Flow and Heat Transfer in Offset Strip and Louvered Fin Heat Exchangers," M.S. Thesis, Department of Mechanical and Industrial Engineering, University of Illinois, Urbana, IL, 1995.
46. Visser, K. D., and Nelson, R. C., "Measurements of Circulation and Vorticity in the Leading Edge Vortex of a Delta Wing," *AIAA Journal*, **31**:104-111, January 1993.
47. Pauley, W. R., and Eaton, J. K., "The Effect of Embedded Longitudinal Vortex Arrays on Turbulent Boundary Layer Heat Transfer," *Journal of Heat Transfer*, **116**:871-879, 1994.
48. Hearch, D., and Baker, M. D., *Computer Graphics*, Prentice-Hall, Inc., Englewood Cliffs, NJ, 1986
49. Arvo, J., *Graphics Gems*, Academic Press, Inc., New York, 1991.
50. Kays, W. M., and London, A. L., *Compact Heat Exchangers*, McGraw-Hill Publishing Co., New York, 1984.
51. Goldstein, R., *Fluid Mechanics Measurements*, Hemisphere Publishing Co., New York, 1983.
52. Fox, R. W., and McDonald, A. T., *Introduction to Fluid Mechanics*, 4th edition, John Wiley & Sons, Inc., New York, 1992.
53. Vargaftik, N. B., *Tables of Thermophysical Properties of Liquids and Gases*, 2nd edition, Hemisphere Publishing Corp., New York, 1975.
54. Biswas, G., Mitra, N. K., and Fiebig, M., "Computational of Laminar Mixed Convection Flow in a Channel with Wing Type Built-in Obstacles," *Journal of Thermophysics*, **3**:447-453, 1989.

55. Biswas, G. and Chattopadhyay, H. "Heat Transfer in a Channel with Built-in Wing-Type Vortex Generators," *International Journal of Heat and Mass Transfer*, **35**:803-814, 1992.
56. Brockmeier, U., Fiebig, M., Guntermann, T., and Mitra, N. K., "Heat Transfer Enhancement in Fin-Plate Heat Exchangers by Wing Type Vortex Generators," *Chemical Engineering Technology*, **12**:288-294, 1989.
57. Bragg, M. B., and Gregorek, G. M., "An Experimental Study of Airfoil Performance with Vortex Generators," *Journal of Aircraft*, **24**:305-309, 1987.
58. Barber, T. J., Mounts, J. S., and McCormick, D. C., "Boundary Layer Energization by Means of Optimized Vortex Generators," *AIAA*, **93-0445**, 1993.
59. Pearcy, H. H., *Boundary Layer and Flow Control*, vol. 2, Pergamon Press, New York, 1961.